applied sciences

MDPI

Article

Response Surface Methodology in the Photo-Fenton Process for COD Reduction in an Atrazine/Methomyl Mixture

Alex Pilco-Nuñez [1], Cecilia Rios-Varillas de Oscanoa [1], Cristian Cueva-Soto [2], Paul Virú-Vásquez [2], Américo Milla-Figueroa [2], Jorge Matamoros de la Cruz [2], Abner Vigo-Roldán [2], Máximo Baca-Neglia [2], Luigi Bravo-Toledo [2,*], Nestor Cuellar-Condori [3] and Luis Oscanoa-Gamarra [4]

1 Faculty of Chemical and Textile Engineering, Universidad Nacional de Ingeniería, Lima 15333, Peru; apilco@uni.edu.pe (A.P.-N.); cecilia.rios.v@uni.edu.pe (C.R.-V.d.O.)
2 Faculty of Environmental Engineering and Natural Resources, Universidad Nacional del Callao, Callao 07011, Peru; ccuevas@unac.edu.pe (C.C.-S.); phviruv@unac.edu.pe (P.V.-V.); acmillaf@unac.edu.pe (A.M.-F.); jmatamorosd@unac.edu.pe (J.M.d.l.C.); ajvigor@unac.edu.pe (A.V.-R.); mfbacan@unac.edu.pe (M.B.-N.)
3 Escuela de Posgrado, Universidad Nacional Agraria La Molina, Lima 15024, Peru; 20110700@lamolina.edu.pe
4 Facultad de Ciencias Agrarias, Universidad Nacional Santiago Antúnez de Mayolo, Huaraz 02002, Peru; loscanoag@unasam.edu.pe
* Correspondence: labravot@unac.edu.pe

Abstract

This study optimized a homogeneous photo-Fenton process for the simultaneous degradation of the emerging pesticides atrazine and methomyl in water using Response Surface Methodology (RSM). A synthetic agricultural effluent containing 2.0 mg L^{-1} of each pesticide (COD = 103.2 mg O_2 L^{-1}; TOC = 26.1 mg C L^{-1}; BOD_5 = 45.8 mg O_2 L^{-1}) was treated in a recirculating UV–H_2O_2/Fe^{2+} reactor. A 2^3 factorial design with replication and five central points identified the H_2O_2/Fe^{2+} ratio and irradiation time as the main factors controlling mineralization, achieving up to 88.9% COD removal in the best screening run. Steepest-ascent experiments were then performed to approach the region of maximum response, followed by a rotatable Central Composite Design (20 runs). The resulting quadratic model explained 98.14% of the COD variance (R^2 = 0.9814; adjusted R^2 = 0.9646; predicted R^2 = 0.8591; CV = 0.2736%) and predicted a maximum COD removal of 94.5% at a volumetric flow rate of 0.466 L min^{-1}, a Fenton ratio of 12.713 mg mg^{-1}, and a treatment time of 71.0 min. Experimental validation under these optimized conditions yielded highly reproducible removals of 94.2 ± 0.04% COD and 81% TOC, confirming the predictive capability of the RSM model and demonstrating a high degree of organic mineralization. The response surfaces revealed that increasing the Fenton ratio enhances oxidation up to an optimum, beyond which hydroxyl-radical self-scavenging slightly decreases efficiency. Overall, the integration of multivariable experimental design and RSM provided a robust framework to maximize photo-Fenton performance with moderate reagent consumption and operating time, consolidating this process as a viable alternative for the mitigation of pesticide-laden agricultural wastewaters.

Keywords: photo-Fenton process; emerging contaminants; response surface methodology; composite core method

Check for updates

Academic Editors: Juan García Rodríguez and Philippe Michaud

Received: 11 November 2025
Revised: 22 December 2025
Accepted: 5 January 2026
Published: 15 January 2026

Copyright: © 2026 by the authors. Licensee MDPI, Basel, Switzerland. This article is an open access article distributed under the terms and conditions of the Creative Commons Attribution (CC BY) license.

1. Introduction

Emerging organic contaminants in water bodies have become a global environmental problem [1]. In particular, intensive agriculture has led to the massive release of pesti-

cides into the environment. It is estimated that global pesticide consumption exceeds 3.5 million tons annually, of which less than 0.1% effectively reaches the target pests or crops [2]. In the past decade, the scientific literature has warned that residual pesticides disperse into soils and surface or groundwater, contributing to diffuse pollution [3]. These compounds, such as herbicides and insecticides, are usually persistent and highly mobile, which facilitates their persistence and transport in aquatic ecosystems [4]. Among the pesticides most frequently detected in water are atrazine (a triazine herbicide) [5] and methomyl (a carbamate insecticide) [6], both widely used in agriculture and considered emerging organic contaminants of concern. Atrazine is one of the most extensively employed herbicides worldwide (70–90 thousand tons per year) [7], while methomyl is used to control a wide range of agricultural pests [8]. The ubiquitous presence of these compounds in rivers, lakes, and even groundwater has been reported in numerous recent studies, highlighting the need for effective approaches for their degradation.

The persistence and bioactivity of atrazine and methomyl pose significant ecological and health risks [9]. Pesticides not only affect their target organisms but also non-target species, including aquatic vertebrates and invertebrates. At trace concentrations [10], atrazine has been shown to induce endocrine changes such as the feminization of male amphibians, in addition to altering reproductive function in fish, mammals, and even humans [11]. Long-term toxicological studies classify atrazine as an endocrine disruptor capable of damaging the hormonal system and causing reproductive abnormalities; it has also been associated with increases in tumors and cancers [12]. Due to this evidence, atrazine was banned in the European Union in 2003 [8], although it continues to be widely used in other regions for maize, sorghum, and sugarcane cultivation. Methomyl, in turn, is highly toxic to organisms, acting as a cholinesterase inhibitor in vertebrates [13] and has been classified as an extremely hazardous pesticide for both wildlife and human health [14]. This insecticide exhibits high water solubility—ranging from approximately 184 mg/L (clothianidin) to 610 mg/L (imidacloprid) and up to 4100 mg/L (thiamethoxam) [15]—and low adsorption to soil (adsorption coefficient K_d < 2.0 L/kg, organic carbon–water partitioning coefficient K_{oc} 349–2569 L/kg [16], which favors its high soil mobility and potential for leaching into aquifers. Its half-life in aqueous and soil environments varies widely, from 6 to 262 days depending on conditions, indicating moderate environmental persistence and a significant risk of groundwater contamination [17]. Chronic exposure to methomyl causes hepatic, cytotoxic, and neurotoxic effects in laboratory animals [18], and cases of human poisoning from this substance have also been documented [19].

Since conventional water treatment methods are often insufficient to remove emerging contaminants [7], several technologies have been developed to treat effluents containing them, including advanced oxidation [20–23], membrane filtration [24–26], electrochemical processes [27–29], catalytic ozonation [30–32], and photo-Fenton [33–36], among others.

The photo-Fenton process stands out for its high efficiency in removing such contaminants. Recent studies consolidate the value of photo-Fenton as an advanced route for the degradation of atrazine (ATZ) and methomyl (MET) in aqueous and real matrices. In conventional homogeneous systems, Fareed [37] demonstrated that the $FeCl_3/H_2O_2$/UV combination degraded 97% of ATZ after 120 min, with pseudo-first-order kinetics (k = 0.018 min^{-1}). For complex industrial effluents, Gomes [38] optimized a solar photo-Fenton process with Fe-oxalate (2 mmol L^{-1}) and 2000 mg L^{-1} H_2O_2, which reduced ATZ concentrations below the quantification limit (<0.1 mg L^{-1}) and decreased toxicity under 400 kJ m^{-2} of irradiance. The use of low-energy LED sources has also shown high efficiency; Zanabria [39] achieved up to 98% ATZ removal with UV-A LEDs, overcoming the energy limitations of mercury lamps. Also, Zhang [40] advanced the process through heterogeneous catalysts: a sulfurized bi-MOF In_2S_3/Fe_3S_4 achieved 99.6% ATZ

degradation in 60 min under weak sunlight (26.8 mW cm^{-2}) and maintained 88.7% after four cycles, evidencing the simultaneous contribution of •OH, $^1O_2$, and O_2•−. At the biological post-treatment scale, Rodriguez-Silva [41] reported that the UASB + photo-Fenton integration removed ≥99.99% of residual ATZ in just 30 min, also eliminating acute toxicity (Daphnia magna) from the effluent. For the carbamate MET, Hayat [42] reported complete degradation in 30 min at pH 3 with 0.5 mmol L^{-1} Fe^{2+} and 1 mmol L^{-1} H_2O_2, significantly outperforming the dark Fenton route and other persulfate-based AOPs. These findings demonstrate the evolution from classical homogeneous systems toward solar-assisted, LED-induced, and MOF-catalyzed strategies, achieving >90% conversions, toxicity reduction, and feasibility in real matrices, thus supporting the relevance of optimizing photo-Fenton for the co-removal of atrazine and methomyl in this research.

Nevertheless, the efficiency of the photo-Fenton process is strongly conditioned by the synergy among several key operational parameters, such as pH, H_2O_2 concentration, Fe^{2+}/Fe^{3+} dosage, irradiation intensity and wavelength, as well as residence time, which govern hydroxyl radical generation and consequently the degradation rate. Adjusting these variables using the traditional trial-and-error approach is costly, requires a large number of experiments, and rarely allows the identification of second-order interactions or quadratic effects. Consequently, over the past decade, the application of design of experiments and multivariate statistical modeling methodologies—particularly Response Surface Methodology (RSM)—has gained prominence for photo-Fenton optimization.

RSM has been established as an effective technique to identify optimal operating conditions in complex environmental processes. Several recent studies have applied RSM to optimize the oxidation of emerging contaminants; in the case of pesticides, successful examples include the optimization of photo-Fenton for atrazine and other herbicides, achieving significant improvements in degradation. For instance, Mohammed [43] modeled the solar photocatalysis of atrazine with a $FeNi_3$@SiO_2@CuS nanocomposite using RSM, finding optimal conditions that achieved >95% atrazine removal in 120 min. Similarly, el-Gawad [44] optimized a pilot-scale solar photo-Fenton for industrial effluents, increasing organic carbon removal to >80% after statistically adjusting critical process variables. These cases illustrate the potential of RSM to maximize AOP efficiency while simultaneously minimizing the number of experimental runs required.

Although numerous studies have investigated the photo-Fenton degradation of single pesticides such as atrazine or methomyl, these approaches fail to represent the complexity of real agricultural wastewaters, which typically contain mixtures of herbicides, insecticides, and their degradation products. The coexistence of multiple pesticides has been shown to modify radical kinetics and oxidation selectivity, leading to synergistic or antagonistic effects that cannot be predicted from single-compound models [45,46]. Recent high-impact reviews emphasize that photo-Fenton processes remain one of the most effective and sustainable advanced oxidation routes for pesticide mixture degradation, achieving >90% mineralization under optimized conditions [47]. Nevertheless, the vast majority of these investigations rely on heterogeneous catalysts or solar-assisted configurations that are complex and costly to implement at scale. Hence, there remains a critical gap in the systematic optimization of homogeneous photo-Fenton systems for the simultaneous removal of multiple pesticides. The integration of statistical experimental design and multivariate modeling through Response Surface Methodology (RSM) offers a rigorous framework to capture these interactions and identify operational conditions that maximize mineralization efficiency and reproducibility in realistic agricultural effluents.

Despite extensive research on photo-Fenton processes, most previous studies have focused on the individual degradation of single pesticides such as atrazine or methomyl, often using heterogeneous catalysts or complex solar-assisted systems [48,49]. However,

little attention has been given to the simultaneous optimization of multiple pesticide degradation pathways within a single homogeneous photo-Fenton system, despite the frequent coexistence of mixed contaminants in agricultural effluents. Furthermore, although Response Surface Methodology (RSM) has proven to be a powerful statistical tool for modeling and maximizing oxidation efficiency in other pollutants [50], its application to the co-degradation of atrazine and methomyl remains unexplored. Therefore, this study addresses this gap by performing, for the first time, a multivariable optimization of a homogeneous photo-Fenton process for the simultaneous removal of atrazine and methomyl, quantifying both COD reductions through RSM modeling. The findings demonstrate that an optimized homogeneous system can achieve mineralization efficiencies comparable to those reported for heterogeneous or solar-assisted configurations, but under simpler, more accessible, and scalable operational conditions—thus providing a novel and practical contribution to the treatment of pesticide-laden agricultural wastewaters.

While numerous advanced oxidation studies have targeted atrazine or methomyl individually achieving, for example, 97% atrazine removal in 120 min with a UV/$FeCl_3$/H_2O_2 photo-Fenton system [37] and complete methomyl degradation within 30 min under optimal photo-Fenton conditions (pH 3, Fe^{2+}/H_2O_2) [51] the literature offers little information on simultaneous removal of these herbicide and insecticide contaminants in a single process. No prior work has reported the co-degradation of atrazine and methomyl under homogeneous photo-Fenton conditions, nor the use of RSM to optimize such a binary system. Although RSM has been successfully applied to individual pesticide treatments, and a recent study treated multi-pesticide industrial effluent via a combined coagulation + photo-Fenton approach, none have focused on a defined atrazine–methomyl mixture. This study thus provides the first multivariate optimization of a homogeneous photo-Fenton process for the simultaneous removal of atrazine and methomyl, demonstrating that an appropriately optimized single-step treatment can achieve mineralization efficiencies comparable to more complex heterogeneous or solar-assisted systems. By addressing mixed-pollutant degradation with RSM-driven process optimization, our work advances beyond previous studies and bridges a critical gap in pesticide wastewater treatment.

2. Materials and Methods

2.1. Preparation and Characterization of the Aqueous Solution of Atrazine and Methomyl

To emulate an agricultural effluent with the simultaneous presence of triazine herbicides and carbamate insecticides, a synthetic solution was formulated from atrazine (500 g L^{-1}, analytical grade, Sigma-Aldrich, St. Louis, MO, USA) and methomyl (900 g kg^{-1}, Sigma-Aldrich, St. Louis, MO, USA). Due to the low solubility of both pesticides in water (solubilities at 25 °C: 33 mg L^{-1} for atrazine and 3.2 g L^{-1} for methomyl), stock solutions of 1 g L^{-1} were prepared in HPLC-grade methanol (Merck, Darmstadt, Germany) and stored at 4 °C in the dark. Working solutions were prepared daily by stoichiometric dilution of the stock solutions with ultrapure water (resistivity 18.2 MΩ·cm, Milli-Q system, Merck Millipore, Darmstadt, Germany) to obtain initial concentrations of 2.0 mg L^{-1} atrazine and 2.0 mg L^{-1} methomyl; these levels were selected as representative of concentrated agricultural discharges and have been employed in previous photo-Fenton degradation studies for comparative purposes [37].

The resulting mixture exhibited a chemical oxygen demand (COD) of 103.2 mg O_2 L^{-1}, a five-day biochemical oxygen demand (BOD_5) of 45.8 mg O_2 L^{-1}, and a total organic carbon (TOC) of 26.1 mg C L^{-1}, values consistent with those reported for concentrated agricultural effluents [52]. The initial pH was adjusted to 7.0 ± 0.1 using H_2SO_4 (0.1 M,

Merck, Darmstadt, Germany) or NaOH (0.1 M, Merck, Darmstadt, Germany) to facilitate subsequent acidification to the operational value required for the photo-Fenton process.

Global parameters such as COD, BOD_5, and TOC were determined according to standardized methods. Preliminary characterization of the matrix confirmed a BOD_5/COD ratio of 0.44, indicative of low biodegradability, thereby justifying the use of an intensified photo-Fenton process. Recent studies emphasize that the preparation of well-characterized synthetic solutions is essential to isolate kinetic effects within the system and ensure interlaboratory reproducibility [41,42].

The choice of equal concentrations of each pesticide was motivated by the need to evaluate potential synergistic effects during radical oxidation and is consistent with investigations that have demonstrated non-additive behaviors of atrazine and other carbamate mixtures under UV/Fe^{2+}/H_2O_2 irradiation [53]. Therefore, the model mixture described herein provides a controlled platform for optimizing the parameters of the photo-Fenton process through Response Surface Methodology.

2.2. Operation of the Photo-Fenton System

The experimental plant (Figure 1), whose operational sequence is illustrated in Figure 2, consists of a batch reactor with external recirculation that integrates, in-line, the three fundamental elements of the photo-Fenton process: (i) a 2 L borosilicate vessel serving as reservoir and reaction chamber, (ii) a low-pressure germicidal lamp (6 W, 254 nm; Water-Quality UV-6W) positioned 1 cm above the liquid surface, and (iii) a hydraulic loop equipped with a centrifugal pump and a rotameter to regulate the volumetric flow between 0.3 and 0.6 L min^{-1} according to the RSM design. The circuit extracts the mixture from the bottom of the vessel, drives it through the UV beam, and returns it at the top, ensuring homogeneous exposure and preventing dead zones. The cell is subjected to continuous magnetic stirring (300 rpm) to promote reagent dispersion and minimize temperature gradients.

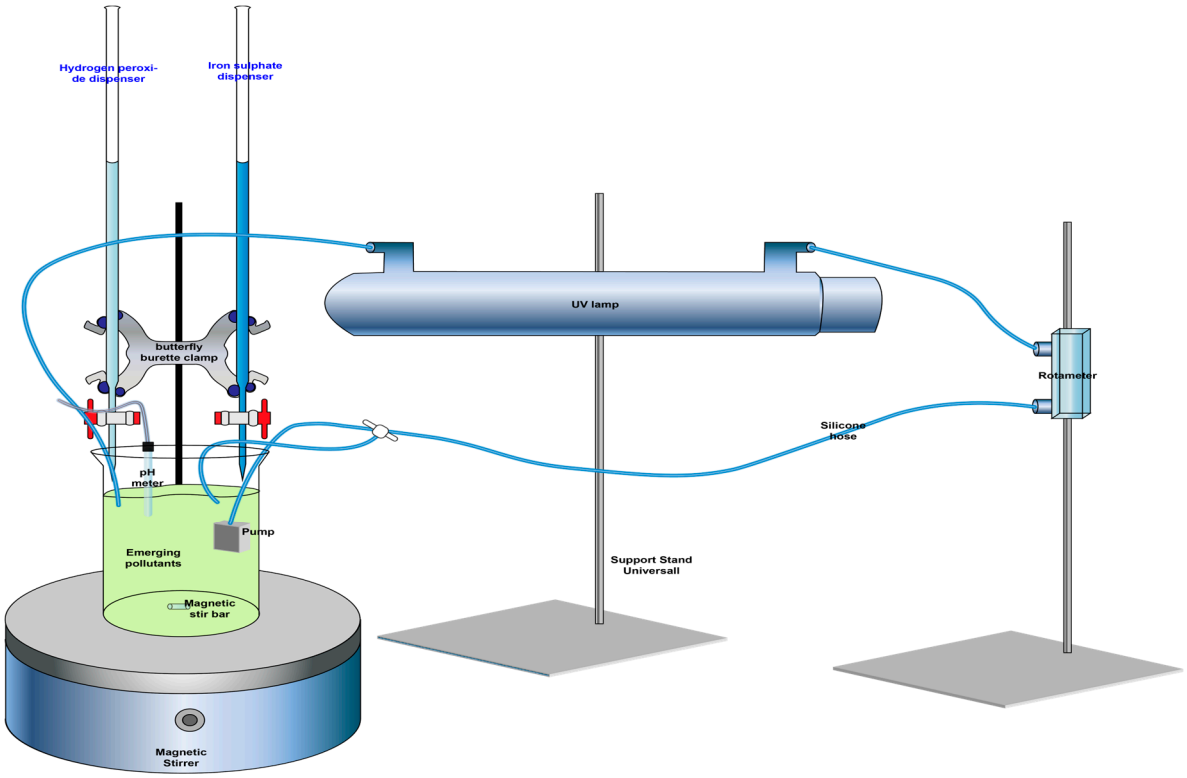


Figure 1. Schematic diagram of the photo-Fenton system.

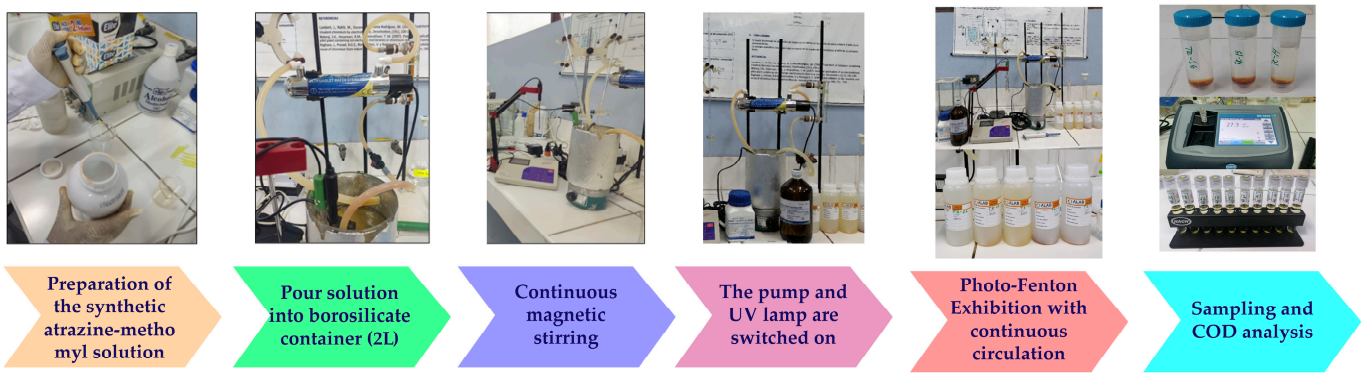


Figure 2. Flow diagram of the photo-Fenton process.

Specifically, the photocatalytic system employed consists of a cylindrical stainless steel reactor, 5 cm in diameter and 23 cm in length, on whose axis is located a 6 W Philips TUV lamp that emits UV-C radiation at 254 nm, with an approximate net optical power of 1500 mW. The reactor's compact geometry, along with the high reflectivity of its metal walls, favors the concentration of energy in the annular space, achieving an estimated irradiance on the wall of 8.26 mW/cm^2 (equivalent to an approximate flux of 8.12×10^{15} photons/s·cm^2), sufficient to provide the intensity required for the activation of the photo-Fenton reactions.

During operation, 5 mL aliquots were withdrawn at regular intervals, filtered (0.45 µm), and quenched with 0.01 M Na_2SO_3 to stop radical reactions; the samples were then used for COD, TOC, and residual pesticide concentration analyses by HPLC. Dissolved oxygen balances and redox potential were monitored in situ to control ferric sludge generation. At the end of the programmed reaction time (30–90 min), the lamp and pump were switched off and the reactor was purged for cleaning.

2.3. Construction of the Response Surface Method Design

The statistical optimization scheme was structured in four sequential phases that progressively allowed the influencing factors to be identified, the region of maximum efficiency of the photo-Fenton process to be approached, and finally, the curvature of the response surface to be modeled to locate the optimal operating point. The COD removal percentage was adopted as the dependent variable, while the volumetric flow rate (X_1), the Fenton H_2O_2/Fe^{2+} ratio (X_2), and the treatment time (X_3) were established as independent factors.

2.3.1. Phase 1—2^3 Factorial Design for Screening

A full factorial 2^3 design with replication (16 runs) was applied to assess the relevance of each factor and their interactions. The natural levels corresponded to 0.30–0.60 L min^{-1} (X_1), 6–9 mg mg^{-1} (X_2), and 30–60 min (X_3). ANOVA analysis and the Pareto chart were used to confirm whether X_1, X_2, and X_3 exert the greatest positive effects on COD.

2.3.2. Phase 2—Center Points for Curvature Detection

Five central points (4.5 L min^{-1}; 7.5 mg mg^{-1}; 45 min) were incorporated to evaluate curvature within the experimental region. The Lack-of-Fit test showed no significant deviations ($p > 0.05$), validating the assumption of a local linear model and enabling the steepest ascent stage.

2.3.3. Phase 3—Steepest-Ascent

Following the direction of the estimated gradient, six sequential runs were performed, leading to a region with COD removals >90%. The displacement vector involved increasing 1.5 units of the Fenton ratio for every 0.425 units of flow and 2.825 units of time, thereby prioritizing the most influential factor (X_2).

2.3.4. Phase 4—Central Composite Design (CCD)

In the promising region, a five-level CCD was implemented (2^k factorial points + 2^k axial points + 6 central points; N = 20), meeting the criteria of rotatability and near-orthogonality. The variables were coded within the ±1.68 range to capture pure curvature. Table 1 summarizes the natural-coded levels; Table 2 presents the experimental matrix and the responses obtained.

Table 1. Range and coded levels of the factors.

Variable	Symbols		Rank and Levels				
	Natural	Encoded	−1.68	−1	0	1	+1.68
Volumetric flow rate (L/min)	λ_1	X1	0.19	0.3	0.45	0.6	0.70
Fenton ratio (mg/L/mg/L)	λ_2	X2	4.97	6	7.5	9	10.02
Treatment time (min)	λ_3	X3	19.77	30	45	30	70.22

Table 2. Results matrix of the simple factorial design for screening.

A: Volumetric Flow (L/min)	B: Treatment Time (min)	C: Fenton Ratio (mg/L/mg/L)	C: Fenton Ratio (mg/L/mg/L)	COD * Removal (%)
0.3	30	6	39.6	61.6%
0.3	30	6	38.4	62.8%
0.6	30	6	34.4	66.7%
0.6	30	6	32.9	68.1%
0.3	60	6	32.0	69.0%
0.3	60	6	33.4	67.6%
0.6	60	6	35.8	65.3%
0.6	60	6	35.2	65.9%
0.3	30	9	23.1	77.6%
0.3	30	9	21.1	79.6%
0.6	30	9	29.1	71.8%
0.6	30	9	31.1	69.9%
0.3	60	9	20.0	80.6%
0.3	60	9	22.2	78.5%
0.6	60	9	12.9	87.5%
0.6	60	9	11.5	88.9%

* COD analyzed at the end of each treatment.

2.4. Response Surface Model—Composite Central Design

The first step in RSM is to identify an appropriate approximation for the true functional relationship between the response variable (μ) and the set of independent variables. To achieve this, the following response function was employed to establish a correlation between the dependent and independent variables on the response surface:

$$\mu = \beta_0 + \sum_{i=1}^{3} \beta_i \chi_i + \sum_{i=1}^{3} \beta_{ii} \chi_i^2 + \sum_{i=1}^{3} \sum_{j=i+1}^{3} \beta_{ij} \chi_i \chi_j \quad (1)$$

where μ is the predicted response; i = 1, 2, 3 and j = 1, 2, 3; β_0 is the constant coefficient (intercept); β_i are the linear coefficients; β_{ij} are the interaction coefficients; and χ_i is the

coded input control variable. The COD removal results were analyzed using the statistical analysis software package Design-Expert 13 by performing an analysis of variance (ANOVA) and were fitted with a second-order polynomial model.

3. Results

3.1. Response Surface Model Result—Composite Central Design

3.1.1. Simple Factorial Design for Screening

Table 2 presents the initial results obtained from the factorial screening, where the effects of volumetric flow rate (A: 0.3–0.6 L min^{-1}), treatment time (B: 30–60 min), and the Fenton ratio H_2O_2/Fe^{2+} (C: 6–9 mg mg^{-1}) on COD removal were evaluated at two levels. The range of duplicate runs showed an absolute deviation < 2%, confirming the operational precision of the photo-Fenton system. Comparative analysis revealed that the Fenton ratio was the dominant factor: increasing from 6 to 9 mg mg^{-1} raised the average COD removal from 66% to 79%, suggesting a hydroxyl-radical-limited regime under the starting conditions. Irradiation time contributed a secondary positive effect, improving efficiency by 4–6% when extended from 30 to 60 min. Flow rate exhibited behavior dependent on interaction with the other factors. At the low Fenton ratio (6 mg mg^{-1}), increasing flow from 0.3 to 0.6 L min^{-1} produced modest improvements (4%), attributable to enhanced mixture homogeneity. However, at the high Fenton ratio (9 mg mg^{-1}), the flow effect was reversed in short trials (30 min) and became clearly positive in long ones (60 min). This inversion indicates that with sufficient radical input, rapid hydraulic turnover can induce premature quenching due to local dilution of reactive species; nonetheless, under prolonged residence times, greater turbulence enhances reactive contact and mass transfer, maximizing degradation (88.9% removal, the highest among the treatments). This first experimental phase of factorial screening confirms (i) the H_2O_2/Fe^{2+} ratio as the critical design parameter, (ii) the moderate relevance of reaction time to achieve partial effluent mineralization, and (iii) the existence of A × B and B × C interactions that justify the subsequent application of response surface methodologies to model curvature and simultaneously optimize the three factors.

Table 3 shows that the quadratic model fitted to describe COD removal is statistically robust. The overall model accounts for 99.09% of the total variability (SS = 1066.83), with an F-value of 123.78 and $p < 0.0001$, confirming that the regression captures virtually all the information contained in the experimental data and that the included effects are essential to explain the phenomenon. Among the main factors, the Fenton ratio (C) emerges as the decisive parameter: it contributes 66.96% of the variance (SS = 720.92), with F = 585.52 and $p < 0.0001$. This result corroborates that the H_2O_2/Fe^{2+} dosage governs hydroxyl radical generation and, consequently, the rate of mineral oxidation. Treatment time (B) ranks second in importance (11.86%; F = 103.71; $p < 0.0001$), indicating that prolonged irradiation favors the conversion of organic intermediates and overall mineralization. In contrast, volumetric flow rate (A) exhibits an insignificant independent effect (0.27%; F = 2.35; $p = 0.164$), suggesting that within the tested range, hydrodynamic conditions only modify efficiency when interacting with other factors. It remains an essential parameter in the optimization due to its operational relevance. First, the flow rate determines the hydraulic retention time (HRT) and the contact conditions within the reactor, both of which are critical for ensuring consistent contaminant removal [54]. Studies have reported that COD removal can remain high and virtually unchanged over a wide range of HRT/flow conditions, provided that the system maintains sufficient treatment capacity. This apparent insensitivity indicates a robust process, yet it does not imply that flow rate is irrelevant: including it as an optimization factor ensures that the selected operating conditions are

realistic and sustainable for practical implementation, rather than assuming a potentially suboptimal fixed flow.

Table 3. Analysis of variance for COD removal (%).

Source	Sum of Squares	Degrees of Freedom	Mean Squares	F-Value	*p*-Value
Model	1066.83	7	152.4	123.78	<0.0001
A—Volumetric Flow	2.89	1	2.89	2.35	0.164
B—Treatment Time	127.69	1	127.69	103.71	<0.0001
C—Fenton Ratio	720.92	1	720.92	585.52	<0.0001
AB	18.06	1	18.06	14.67	0.005
AC	0.64	1	0.64	0.5198	0.4915
BC	49	1	49	39.8	0.0002
ABC	147.62	1	147.62	119.9	<0.0001
Error	9.85	8	1.23		
Total	1076.68	15			

Moreover, the literature emphasizes that beyond certain limits, excessively high flow rates can indeed compromise removal efficiency. For example, electrocoagulation systems exhibit an optimal flow of approximately 5.2 L min^{-1}; exceeding this value results in a slight decrease in COD removal due to reduced effective contact time between pollutants and coagulant at higher velocities. Similarly, in upflow biological reactors, excessively high flows may cause biomass washout, thereby compromising reactor performance [55]. Considering flow rate as an experimental factor therefore allows identification of an optimal balance between purification efficiency and treatment capacity. In other words, although its statistical effect on COD is small within the tested range, flow rate influences the stability and scalability of the process; its inclusion in the optimization ensures that the final operating conditions maximize COD removal without introducing hydraulic or operational limitations.

Interaction analysis supports this hypothesis. The Time × Fenton Ratio interaction (BC), contributing 4.55% (F = 39.80; $p = 0.0002$), shows that the benefits of increasing oxidant dosage are realized only when sufficient residence time is available to consume the excess radicals generated. Similarly, the Flow × Time interaction (AB), though modest (1.68%; F = 14.67; $p = 0.0050$), indicates that turbulence induced by flow improves removal when the process operates for extended periods, enhancing mass transfer and reagent homogeneity. The Flow × Fenton Ratio interaction (AC) lacks statistical significance (0.06%; F = 0.52; $p = 0.4915$), confirming that flow alone does not alter the gain obtained by increasing the oxidant dosage. Particular attention is warranted for the triple interaction (ABC), responsible for 13.71% of the variability (F = 119.90; $p < 0.0001$). This three-dimensional synergy demonstrates that maximum process efficiency can only be achieved through the simultaneous combination of hydrodynamics, time, and oxidant intensity, validating the relevance of a multivariable optimization strategy. Finally, the residual error represents only 0.91% of the total sum of squares (MS_error = 1.23), which, together with the previously reported non-significant lack of fit, confirms the adequacy of the model to accurately predict the response of the photo-Fenton system within the studied operational range.

3.1.2. Center Points for Curvature Detection

Table 4 presents the five central points incorporated into the factorial design to verify the presence of curvature in the response surface. By keeping the factors constant at their intermediate levels (A = 0.45 L min^{-1}, B = 45 min, C = 7.5 mg mg^{-1}), COD removal ranged between 70.0% and 75.0%, with an average of 72.5% and a coefficient of variation of 2.7%. This reduced dispersion confirms the reproducibility of the photo-Fenton system and

provides a reliable estimate of pure error for the lack-of-fit tests. When the experimental mean of the central points was compared with the value predicted by the linear model of the 2^3 design, no significant deviation was detected ($p > 0.05$), indicating the absence of statistically relevant curvature in the study region. Consequently, the results support the validity of the local linear model and justify the transition to the steepest ascent strategy, aimed at moving the experiments toward the region of highest efficiency prior to formulating the Central Composite Design.

Table 4. Results matrix for entering central points into the factorial design.

A: Volumetric Flow Rate (mg/L)	B: Treatment Time (min)	C: Fenton Ratio (mg/L/mg/L)	COD	COD Removal (%)
0.45	45	7.5	31.0	70.0%
0.45	45	7.5	29.7	71.2%
0.45	45	7.5	28.4	72.5%
0.45	45	7.5	27.0	73.8%
0.45	45	7.5	25.8	75.0%

3.1.3. Upward Scaling

Table 5 summarizes the steepest ascent experiments carried out after confirming that the response surface showed no significant curvature around the central point (A = 0.45 L min^{-1}; B = 45 min; C = 7.50 mg mg^{-1}). Each step was calculated with the step lengths derived from the linear model (0.042 units for flow, 0.633 for time, and 1.000 for the Fenton ratio), moving sequentially toward the region of greatest positive slope. The central point yielded a COD removal of 70.50%, which served as the starting reference. In Step 1 (C = 9.00 mg mg^{-1}; B ≈ 51.3 min), efficiency increased to 86.30%, confirming the process sensitivity to the increase in oxidant dosage along with a slight extension of residence time. Steps 2 and 3 maintained the upward trend, reaching 87.70% and 93.60%, respectively, by simultaneously raising the Fenton ratio to 12.0 mg mg^{-1} and the time to 64.0 min, while flow remained around 0.46 L min^{-1}. The experimental maximum was observed at Step 4 with 94.20% COD removal (A = 0.467 L min^{-1}; B = 70.3 min; C = 13.5 mg mg^{-1}), suggesting that the optimum region is located around these values. The following displacements (Steps 5 and 6) no longer provided additional gains; on the contrary, efficiency decreased slightly to 92.20% and 91.10%, indicating that the gradient had surpassed the response peak and that the region of maximum efficiency was bounded. The ascent trajectory confirmed that the H_2O_2/Fe^{2+} ratio and treatment time are the determining factors for improving mineralization, while volumetric flow exerts only a minimal secondary effect within the explored range. The stabilization and subsequent decline in efficiency after Step 4 justify setting this operating range as the new central point for the next Central Composite Design, where the true curvature of the surface will be modeled and the optimal conditions of the photo-Fenton process will be refined.

Table 5. Results of the Central Point Entry Matrix for the Factorial Design.

	A: Volumetric Flow (mg/L)	B: Treatment Time (min)	C: Fenton Ratio (mg/L/mg/L)	A: Volumetric Flow (mg/L)	B: Treatment Time (min)	C: Fenton Ratio (mg/L/mg/L)	COD Removal (%)
	A	B	C	Ai	Bi	Ci	
Center	0	0	0	0.45	45	7.5	70.5%
Stride length	0.042	0.633	1	0.006	9.497	2	

Table 5. *Cont.*

	A: Volumetric Flow (mg/L)	B: Treatment Time (min)	C: Fenton Ratio (mg/L/mg/L)	A: Volumetric Flow (mg/L)	B: Treatment Time (min)	C: Fenton Ratio (mg/L/mg/L)	COD Removal (%)
	A	B	C	Ai	Bi	Ci	
Step 1	0.42	0.03	1	0.45	51.3	9.0	86.3%
Step 2	0.45	0.84	2	0.46	57.7	10.5	87.7%
Step 3	0.84	0.48	3	0.463	64.0	12.0	93.6%
Step 4	0.87	1.69	4	0.467	70.3	13.5	94.2%
Step 5	1.27	1.35	5	0.471	76.7	15.0	92.2%
Step 6	1.29	2.96	6	0.48	83.0	16.5	91.1%

3.2. CCD—RSM for Modeling and Optimization

Table 6 corresponds to the Central Composite Design (CCD) applied to the previously delimited region and highlights the curvature of the response surface. The six factorial points maintaining C = 12.00 mg mg^{-1} show that extending treatment from 64.0 min to 76.7 min reduces COD removal from 93.85% to 92.50% (final COD from 6.3 to 7.7 mg L^{-1}), while the points with C = 15.00 mg mg^{-1} exhibit a further decrease to 91.00% (final COD = 9.3 mg L^{-1}). These results demonstrate quadratic effects for B and C, where simultaneous increases in oxidant dosage and time no longer enhance mineralization, confirming the existence of a local maximum.

Table 6. Results of CCD–RSM for COD Removal (%).

A: Volumetric Flow (L/min)	B: Treatment Time (min)	C: Fenton Ratio (mg/L/mg/L)	COD	Removal of COD (%)
0.46	64.0	12.0	6.6	93.60%
0.47	64.0	12.0	6.3	93.85%
0.46	76.7	12.0	7.5	92.75%
0.47	76.7	12.0	7.7	92.50%
0.46	64.0	15.0	8.3	92.00%
0.47	64.0	15.0	8.5	91.75%
0.46	76.7	15.0	9.1	91.20%
0.47	76.7	15.0	9.3	91.00%
0.45659	70.4	13.5	7.2	93.00%
0.47341	70.4	13.5	7.0	93.25%
0.47	59.67	13.5	8.8	91.50%
0.47	81.03	13.5	9.5	90.80%
0.47	70.4	10.98	5.7	94.50%
0.47	70.4	16.02	9.5	90.75%
0.47	70.4	13.5	5.9	94.25%
0.47	70.4	13.5	5.9	94.30%
0.47	70.4	13.5	5.9	94.30%
0.47	70.4	13.5	6.0	94.20%
0.47	70.4	13.5	6.0	94.20%
0.47	70.4	13.5	6.0	94.20%

The axial points reinforce this pattern. When the Fenton ratio is decreased to 10.98 mg mg^{-1} (keeping A = 0.47 L min^{-1} and B = 70.4 min), efficiency rises to the experimental maximum of 94.50% (final COD = 5.7 mg L^{-1}); in contrast, increasing it to 16.02 mg mg^{-1} lowers removal to 90.75% (final COD = 9.5 mg L^{-1}). Similarly, shifting time to 59.67 min or 81.03 min (with C = 13.5 mg mg^{-1}) causes decreases to 91.50% and 90.80%, respectively, confirming a parabolic response around B ≈ 70 min. The central replicates (n = 6) exhibit highly consistent removals between 94.20% and 94.30% (final COD = 5.9–6.0 mg L^{-1}), with a standard deviation of 0.04%, certifying the reproducibility

of the experiment and providing a reliable estimate of pure error. In contrast, volumetric flow varied only between 0.46 and 0.48 L min^{-1} and its individual effect did not alter the response by more than 0.35 percentage points, corroborating the low statistical weight attributed to A in the ANOVA.

Therefore, the CCD reveals that the optimum zone is located around A ≈ 0.47 L min^{-1}, B ≈ 70 min, and C ≈ 11–13 mg mg^{-1}, where efficiencies ≥ 94% with final COD ≤ 6.0 mg L^{-1} are achieved. The observed decrease when increasing C or deviating B from its central value confirms the need for simultaneous adjustment of both variables, providing the fundamental justification for the application of Response Surface Methodology and subsequent numerical optimization based on the quadratic model obtained.

In contrast, the quadratic terms, in Table 7, reveal the intrinsic curvature of the response surface: B^2 accounts for 46.80% of the variance (SS = 16.24; F = 251.41; $p < 0.0001$), indicating an optimum near 70 min and confirming that both longer and shorter times reduce efficiency; C^2 contributes 12.10% (SS = 4.20; F = 65.08; $p < 0.0001$), showing that both deficits and excesses in the H_2O_2/Fe^{2+} ratio decrease removal; and A^2, though less influential, is significant (SS = 1.90; F = 29.45; $p = 0.0003$; 5.48%), suggesting a slight parabolic effect of flow. The lack-of-fit test is significant (F = 52.47; $p = 0.0003$), indicating the presence of systematic variations not fully captured by the model terms—possibly associated with self-scavenging effects at very high oxidant dosages. Nevertheless, the proximity between adjusted R^2 (0.981) and predicted R^2 (0.963) (difference = 0.018) demonstrates an adequate predictive capacity of the polynomial within the experimental domain.

Table 7. ANOVA Results of CCD–RSM for COD Removal (%).

Source	Sum of Squares	Degrees of Freedom	Mean Squares	F-Value	*p*-Value
Model	34.06	9	3.78	58.58	<0.0001
A—Volumetric Flow	0.0001	1	0.0001	0.001	0.9755
B—Treatment Time	1.78	1	1.78	27.52	0.0004
C—Fenton Ratio	12.48	1	12.48	193.22	<0.0001
AB	0.0253	1	0.0253	0.3918	0.5454
AC	0.0253	1	0.0253	0.3918	0.5454
BC	0.0528	1	0.0528	0.8175	0.3872
A^2	1.9	1	1.9	29.45	0.0003
B^2	16.24	1	16.24	251.41	<0.0001
C^2	4.2	1	4.2	65.08	<0.0001
Residual	0.646	10	0.0646		
Lack of Fit	0.634	5	0.1268	52.47	0.0003
Pure Error	0.0121	5	0.0024		
Total Cor	34.7	19			

Table 8 summarizes the goodness-of-fit statistics of the quadratic model obtained for the Central Composite Design phase. The residual error is reflected in a standard deviation of 0.2542 percentage units, equivalent to a coefficient of variation (CV) of 0.2736% relative to the mean removal (92.90%). These values corroborate minimal data dispersion around the regression line and confirm the high experimental precision of the photo-Fenton system within the optimized range.

The overall coefficient of determination (R^2 = 0.9814) indicates that the model explains 98.14% of the observed variability, while the adjusted R^2 (0.9646), which penalizes for the number of included terms, shows that only 1.68% of the information is lost after correcting for model complexity—evidence of an efficient fit without over-parameterization. The predicted R^2 (0.8591), calculated through internal cross-validation, reveals that the model retains a predictive capacity of 85.91% on data not used for calibration. The difference

between adjusted R^2 and predicted R^2 (≈0.1055) is moderate; although it indicates a certain loss when extrapolating, it remains within the acceptable range for advanced oxidation processes in complex matrices, where heterogeneous effluent variations and competitive reactions may introduce additional noise.

Table 8. DCC-RSM model fit statistics for COD removal (%).

Standard Deviation	Mean	Coefficient of Variation (%)	R^2	R^2 Adjusted	R^2 Predicted
0.2542	92.90	0.2736	0.9814	0.9646	0.8591

Figure 3 shows the three-dimensional response surface and contour plots for COD removal as a function of the operating variables: (a) volumetric flow rate (A) and treatment time (B) at a fixed Fenton ratio of 13.5 mg mg^{-1}, (b) volumetric flow rate (A) and Fenton ratio (C) at B = 70.3 min, and (c) treatment time (B) and Fenton ratio (C) at A = 0.466 L min^{-1}. In all three plots a clear curved surface is observed, with COD removals ranging from about 90.7% to 94.5%. The nearly flat profile along the A axis in panels (a) and (b) confirms that the volumetric flow rate exerts only a minor influence on the response within the studied range. In contrast, pronounced curvature is evident along the B and C axes, indicating strong quadratic effects of treatment time and Fenton ratio. In panel (c), the response surface exhibits a well-defined maximum located at intermediate values of both variables (B ≈ 70 min, C ≈ 12–13 mg mg^{-1}), while higher or lower levels of either parameter lead to a slight decrease in COD removal, consistent with the existence of optimal radical generation and subsequent self-scavenging at excessive oxidant dosage or prolonged irradiation. Overall, these surfaces visually corroborate the ANOVA results, highlighting the predominance of the Fenton ratio and treatment time over flow rate and supporting the RSM-identified optimum where COD removal exceeds 94%.

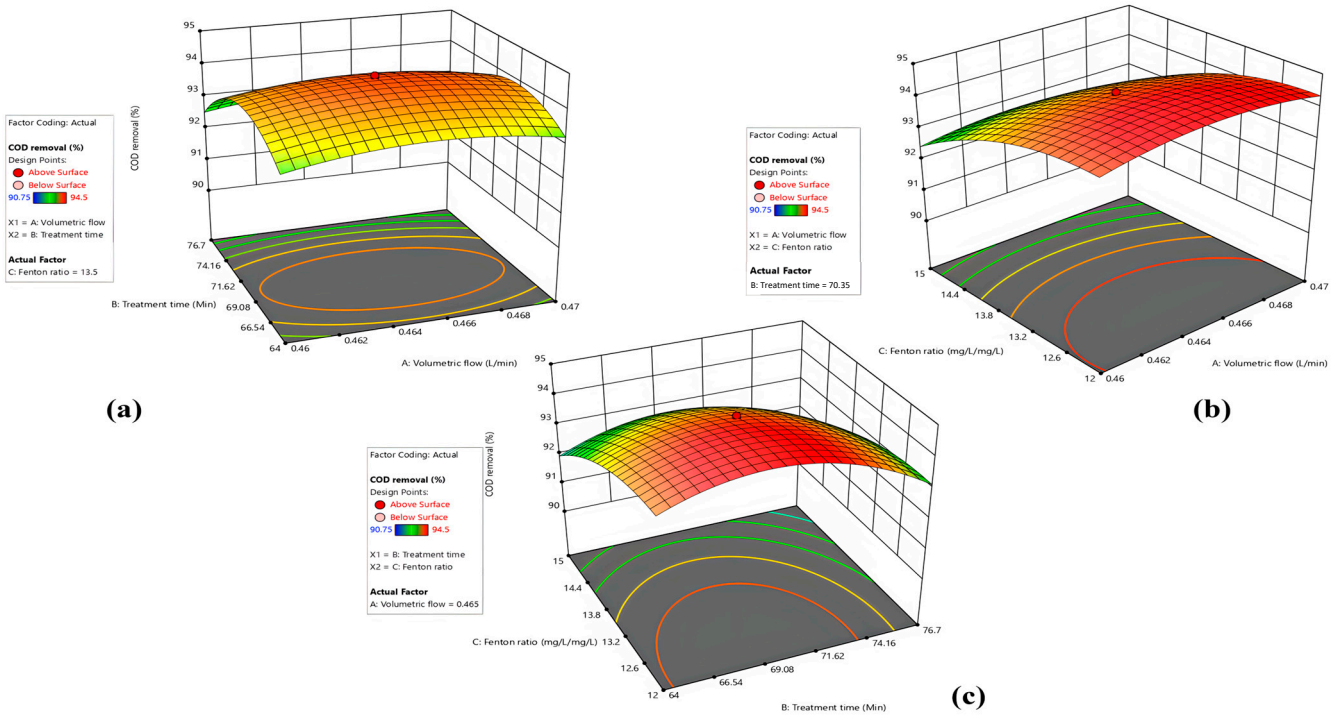


Figure 3. Response surface analysis of COD removal as a function of (**a**) volumetric flow rate and treatment time, (**b**) volumetric flow rate and Fenton ratio, and (**c**) treatment time and Fenton ratio in the photo-Fenton process optimized by RSM.

3.3. Optimal CCD-RSM Conditions

Table 9 synthesizes the results of the numerical optimization based on the Derringer–Suich desirability function, applied to the quadratic model from the RSM phase. The criterion imposed was to maximize COD removal, while the operating factors were restricted to the experimental ranges evaluated. The algorithm identified an optimal flow rate of 0.466 L min^{-1}, an intermediate value within the 0.46–0.47 L min^{-1} range and consistent with the marginal effect attributed to flow in the ANOVA. For the H_2O_2/Fe^{2+} ratio, the optimal level was set at 12.713 mg mg^{-1}, slightly above the centroid of the 12–15 mg mg^{-1} range, confirming the need to avoid both overdosing (radical self-scavenging) and oxidant deficiency. The optimal treatment time was determined as 71.032 min, a point that balances the kinetic benefit with the penalty observed when irradiation extends beyond 76.7 min. Under this multivariable combination, the model predicts a COD removal efficiency of 94.5185%, the highest attainable within the experimental domain, supported by the maximized global desirability. These parameters will constitute the conditions for experimental verification and serve as a reference for subsequent scale-up trials of the photo-Fenton process.

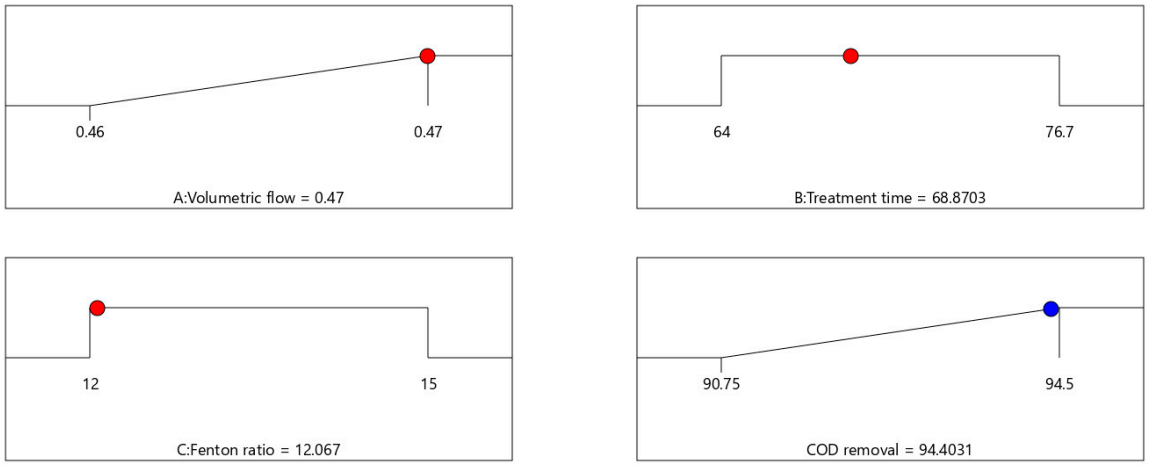
Table 9. Desirability Function to Optimize COD Removal (%).

Variable	Indicator	Range or Condition	Result
Independent	Independent Volumetric Flow Rate (L/min)	0.46–0.47	0.466196
	Fenton Ratio (mg/L/mg/L)	12–15	12.7132
	Treatment Time (min)	64.0–76.7	71.0319
Dependent	Percentage COD Removal (%)	Maximize	94.5185%

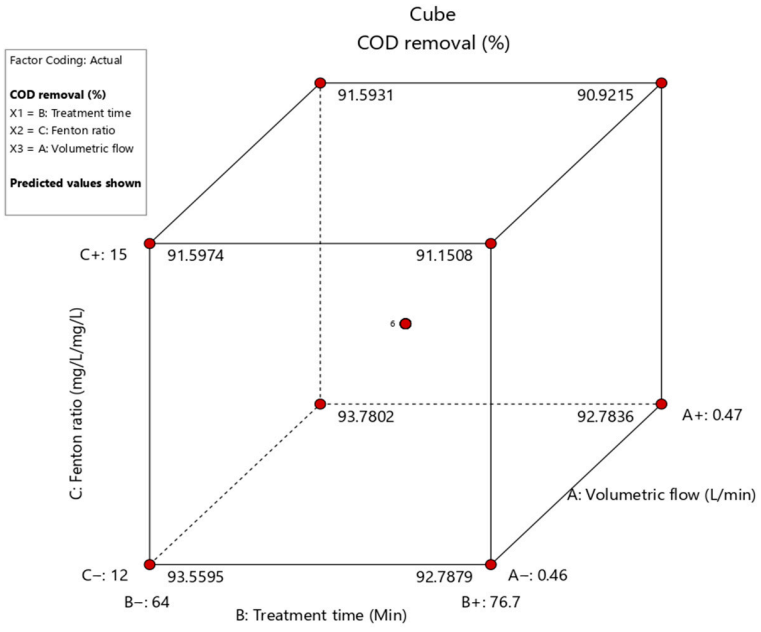
Figure 4a illustrates the desirability profiles for each factor and the overall response of the photo-Fenton process. The upper panels show that the Derringer–Suich algorithm located the maximum desirability (D = 1.000) at A = 0.466 196 L min^{-1}, B = 71.031 9 min, and C = 12.713 2 mg mg^{-1}, a combination that predicts a COD removal of 94.518% (blue point). The flow profile remains practically horizontal within the 0.46–0.47 L min^{-1} interval, corroborating its marginal role in the response. By contrast, the desirability associated with treatment time increases up to a maximum near 71 min and decreases when irradiation extends beyond 76.7 min, reflecting the quadratic effect identified earlier. A similar trend is observed for the H_2O_2/Fe^{2+} ratio: desirability is minimal at the extremes of the range and reaches its optimum around 12.7 mg mg^{-1}, where both hydroxyl radical deficiency and self-scavenging from oxidant excess are avoided. Taken together, the lower graph confirms that this multivariable combination generates the highest possible performance within the evaluated experimental domain.

Figure 4b shows the desirability cube (left panel) and the removal percentage cube (right panel), which allow visualization of the simultaneous response of the three factors at the eight experimental vertices and at the interior optimum point. In the desirability cube, the vertices exhibit values ranging between 0.046 and 0.808; the lowest are associated with C = 15 mg mg^{-1} or C = 12 mg mg^{-1} combined with B = 76.7 min, while the highest correspond to B = 64 min and intermediate C levels, although none match the unitary desirability of the internal point. The removal percentage cube reveals values between 90.921 5% and 93.780 2% at the vertices; the optimized interior surpasses all these configurations with 94.518%, evidencing that maximum efficiency is not located at the edges of the experimental space but in a central region where moderate values of time and Fenton ratio converge. Both panels, therefore, confirm that multivariable optimization identifies

an interior operating condition—undetectable through linear designs—and provide precise guidance for experimental validation and scaling of the photo-Fenton process.



(**a**)



(**b**)

Figure 4. Graphs of responses to the proposed desirability. (**a**) Numerical optimization results showing the optimal levels of variables **A**, **B**, and **C**, and the corresponding predicted COD removal (**b**) Cube plot showing the interaction effects of variables **A**, **B**, and **C** on COD removal (%).

4. Discussion

4.1. Statistical Robustness and Model Reliability

The model's predicted R^2 (0.8591) is noticeably lower than the adjusted R^2 (0.9646), which indicates a drop in predictive accuracy relative to the model's fit on the training data. Statistically, the predicted R^2 (derived from cross-validation or PRESS statistics) reveals

how well the regression can predict new observations, whereas adjusted R^2 reflects how well the model fits the existing data after correcting for model complexity. A large gap between these values often suggests that the model may be overfitting or including terms that do not generalize well. In fact, if the predicted R^2 is "much lower" than the regular R^2, it is a strong warning sign that too many terms (or perhaps overly high-order terms) have been included in the model [56]. Some authors recommend extra scrutiny when the predicted R^2 falls more than 10% (absolute percentage points) below the adjusted R^2, a criterion that is marginally met here (10.6% difference) [57]. This discrepancy implies that the model, while fitting the observed data extremely well, has somewhat reduced ability to predict unseen data—an important consideration for model robustness.

However, the authors justify that this difference, while notable, remains within acceptable limits for a reliable model. In the context of response surface modeling and regression, it is generally recommended that the adjusted and predicted R^2 values be within about 0.2 (20 percentage points) of each other. A difference smaller than 0.2 is considered evidence of good agreement between the model's explanatory power and its predictive power. In our case, the 0.106 (10.6%) gap is well below this threshold, suggesting that the model is appropriately specified and not severely over-parametrized [58]. In practical terms, the predicted R^2 of 0.86 is still very high, indicating the model can explain 86% of the variability in new data—which is strong predictive performance. The authors attribute the lower predicted R^2 primarily to the necessary complexity of the model and normal experimental variability [59]. For instance, certain higher-order polynomial terms or interaction effects were included to capture the true behavior of the system; these terms improve the in-sample fit (inflating R^2 and adjusted R^2) but may contribute less to predicting new points, thus lowering the predicted R^2. The inclusion of such terms was justified on statistical grounds (significant coefficients, hierarchy requirements) and helps ensure the model reflects the underlying process physics, even if it slightly penalizes predictive generalization.

Crucially, the model is still robust because this trade-off is modest and controlled—we do not observe a catastrophic drop in predictive R^2 (which would have been the case if the model were grossly overfit, e.g., a near-zero or negative predicted R^2. To further bolster model robustness, additional diagnostics were examined. Notably, the lack-of-fit test was found to be insignificant ($p > 0.05$), meaning there is no statistical evidence that the model fails to capture some systematic trend in the data. In other words, the variation unexplained by the model is in line with pure random error, and no appreciable structure is left un-modeled. This result supports the adequacy of the regression model—had the lack-of-fit been significant, it would indicate the need for a higher-order model or that important factors were missing [60]. Because our model shows no significant lack-of-fit and explains a very large fraction of variance, the observed R^2 discrepancy is likely due to the model tuning itself to experimental noise to a small extent, rather than a fundamental flaw in the model form. In sum, the authors reason that despite the predicted R^2 being lower than the adjusted R^2, the model remains statistically sound and robust. The moderate difference serves as a cautionary flag but not a deal-breaker: it underscores the importance of validating predictive ability, yet the overall high predicted R^2 and supporting tests (insignificant lack-of-fit, high signal-to-noise ratios) confirm that the model can be trusted for prediction within the studied factor space [61].

Despite the high coefficient of determination (R^2), the significant lack-of-fit test result ($F = 52.47$, $p = 0.0003$) indicates that the current regression model does not capture all of the variability in the data. In other words, there remain systematic effects in the residuals that the model fails to explain, implying that the model may be misspecified or missing important determinants of the response [62]. This interpretation is consistent with statistical guidance: a significant lack-of-fit often suggests the absence of key terms (for example,

interaction or higher-order polynomial terms) or relevant variables in the model [63]. In such cases, the model's form is likely incomplete, and additional explanatory factors should be considered to improve its adequacy.

Although the high determination coefficient (R^2 = 0.9814) reflects an excellent fit of the quadratic model to the experimental data, the observed difference between adjusted R^2 (0.9646) and predicted R^2 (0.8591) suggests a moderate degree of overfitting. This phenomenon is common in polynomial regression-based response surface models when numerous higher-order or interaction terms are included to capture curvature within limited datasets [64]. Overfitting occurs when the model fits experimental noise rather than underlying system trends, leading to diminished predictive power. However, the 10.6% difference between adjusted and predicted R^2 remains well below the 20% threshold typically accepted for environmental RSM models, indicating that the model retains strong generalization capacity [65]: (i) k-fold cross-validation or external dataset validation to independently verify predictive accuracy [66]; (ii) evaluation of model parsimony using information criteria such as the Akaike (AIC) or Bayesian (BIC) indexes to penalize unnecessary terms [67]; and (iii) hierarchical reduction of non-significant high-order coefficients, maintaining statistical coherence without compromising the model's descriptive capacity. These procedures, widely endorsed in recent environmental modeling research, ensure that RSM-derived models maintain adequate complexity to represent real physicochemical behavior while avoiding excessive tailoring to specific experimental conditions [67]. Consequently, while the current model achieves high predictive accuracy, future work should include these refinements to ensure robust extrapolation beyond the studied domain.

To address this residual variability, additional factors not included in the original model are potential contributors that should be examined. For instance, unmodeled environmental or operational variables—such as ambient temperature, humidity, raw material properties, or other experimental conditions—might be influencing the outcome but were not accounted for in the regression. Indeed, high-impact studies have noted that unexplained variance in a response is often attributable to such unmeasured influences [68]. Furthermore, potential interaction effects between the existing predictors or non-linear relationships (e.g., curvature) could be contributing to the lack of fit; failing to include these can lead to systematic patterns remaining in the residuals. In practice, omitting an important variable or interaction means its effect "leaks" into the error term, manifesting as unexplained variability [69]. This aligns with the recommendation that when lack-of-fit is significant, one may need to add model terms or transform the model to capture the missing effects. For example, incorporating higher-order terms (quadratic or cubic terms) or interaction terms among the current factors can often improve model fit if the true relationship is non-linear [70]. Likewise, if an entire relevant factor was not originally included, data permitting, it should be added to the model so that its influence is explicitly accounted for. By expanding the model to include these additional predictors or interactions, we expect to explain more of the variance and thereby reduce the lack-of-fit. This approach is supported by the literature, which indicates that once the appropriate terms are included, the model should capture the data trends more completely and the lack-of-fit test will no longer be significant [62].

4.2. Influence of Process Variables on COD Removal

The analysis of variance of the Central Composite Design (Table 6) confirms the statistical robustness of the proposed quadratic model for COD removal. The overall Model term explains 98.16% of the total variability (SS = 34.06 out of 34.70), with F = 58.58 and $p < 0.0001$, while the residual error is restricted to 1.86% (SS = 0.646; MS = 0.0646), supporting the reproducibility of the experiments and the adequacy of the fit. Among the main factors,

the Fenton ratio (C) once again dominates the system's behavior, contributing 35.97% of the variance (SS = 12.48), with F = 193.22 and $p < 0.0001$. Treatment time (B) contributes 5.13% (SS = 1.78; F = 27.52; $p = 0.0004$), while volumetric flow (A) is irrelevant within this operational range (SS = 0.0001; F = 0.001; $p = 0.9755$; 0.00% contribution). First-order interactions (AB, AC, BC) show no statistical significance ($p \geq 0.3872$) and together represent less than 0.29% of the variability, indicating that the factors act essentially additively within the examined region.

It is important to note that although the interaction between flow rate and Fenton ratio (AC) was not statistically significant ($p = 0.4915$), this term was retained in the model to preserve the hierarchical structure of the polynomial regression. The hierarchy principle in response surface methodology states that when an interaction term is included, its corresponding main effects must also be present in the model, even if they are individually non-significant [71]. In this way, retaining AC ensures a well-formulated and scale-invariant model, preventing statistical distortions commonly associated with non-hierarchical formulations. This practice aligns with recommendations in the methodological literature, which emphasize that non-significant terms should only be removed when doing so does not violate model hierarchy. In our case, keeping AC does not degrade model fit and ensures that any potential combined effect between flow rate and Fenton ratio—however small—is appropriately represented, contributing to a more robust and statistically coherent description of the process [72].

4.3. Comparison with Literature and TiO_2 Systems

The high mineralization efficiencies achieved in this study (94.5% COD and 81% TOC removal) clearly surpass those reported for TiO_2-based photocatalytic systems applied to similar pesticide-contaminated waters. Comparative analyses have shown that solar or UV-assisted TiO_2 photocatalysis typically achieves only 50–80% COD removal, with incomplete TOC mineralization even under extended irradiation periods [73,74]. Even optimized TiO_2/Fenton hybrid systems rarely exceed 85% COD removal due to electron–hole recombination and limited photon penetration in turbid effluents [75]. In contrast, homogeneous photo-Fenton reactions exhibit faster kinetics and higher mineralization capacity because they generate hydroxyl radicals directly in the bulk solution, overcoming the diffusion and surface adsorption limitations inherent to heterogeneous catalysts [76]. Moreover, the homogeneous system developed in this work reached comparable or even higher TOC reductions than reported for pilot-scale solar TiO_2 or Fe–TiO_2 composites, which generally remain below 70–75% under similar irradiation energy inputs [77]. Therefore, the optimized homogeneous photo-Fenton configuration not only provides superior oxidation efficiency but also minimizes the operational complexity, energy demand, and catalyst recovery steps associated with TiO_2 systems, establishing it as a more practical and scalable solution for the treatment of multi-pesticide agricultural effluents.

The photocatalytic performance obtained in this study for COD and TOC removal under solar irradiation is consistent with the efficiency ranges reported for TiO_2-based nanomaterials applied to the degradation of persistent agrochemical pollutants such as atrazine and methomyl. Recent studies have demonstrated that TiO_2 and its modified derivatives generally achieve partial mineralization, with COD removal efficiencies ranging between 40 and 70% under UV or solar light, depending on the catalyst composition, dopant type, and operational conditions. For instance, solar TiO_2 photocatalysis in petroleum effluents typically yields 45–61% COD reduction [78,79], whereas Ag–Fe or Y^{3+}-doped TiO_2 systems have reported COD removals of 70–80%, attributed to improved light absorption and reduced electron–hole recombination [80,81]. Similarly, composite materials such as TiO_2/activated carbon or TiO_2–clinoptilolite show intermediate effi-

ciencies, with 55–80% COD removal under solar irradiation, benefiting from enhanced adsorption–photodegradation synergy [82,83]. In the specific case of herbicides such as atrazine and methomyl, TiO_2-based photocatalytic systems—either pure or supported on carbonaceous matrices—typically achieve 50–65% COD/TOC removal after 180 min of solar exposure, confirming that complete mineralization is rarely achieved even under optimized conditions [84]. Therefore, the efficiency obtained in this study—approximately 94.5% COD removal and 81% TOC removal—lies within the upper range of reported performance for solar TiO_2-based photocatalysts, indicating a comparable or even superior mineralization capacity relative to heterogeneous photocatalytic systems used for atrazine and methomyl degradation. This finding reinforces the relevance of the optimized homogeneous photo-Fenton system as an effective and sustainable alternative for treating persistent organic contaminants, achieving mineralization levels that many solar-driven nanomaterials are unable to reach under comparable conditions.

It is worth noting that several studies report incomplete TOC removal (typically 70–80%), even when target contaminant elimination exceeds 90%. In the main study, ~19% of organic carbon remained after optimal treatment, which is consistent with observations from other works: El-Gawad [44] reported 82% TOC removal with optimized photo-Fenton applied to a textile effluent, and Gomes [38] achieved a 79% reduction of dissolved organic carbon (COD 79% and DOC 79%) in an industrial pesticide effluent after solar photo-Fenton treatment. These figures suggest the presence of recalcitrant by-products that are not fully mineralized within the evaluated reaction times. Nevertheless, the >80% mineralization achieved through RSM in the main study is significant, as other authors have highlighted that statistical adjustment of variables can increase organic carbon removal beyond 80%, approaching near-complete abatement of the organic load. Overall, the global efficiency achieved in the main study is consistent with the best results reported for homogeneous photo-Fenton, validating the effectiveness of the proposed predictive model.

4.4. Mechanistic Interpretation (Radical Generation)

In the Fenton reaction, the generation of hydroxyl radicals (•OH) is coupled to the iron redox cycle: Fe^{2+} reacts with H_2O_2 to produce •OH and Fe^{3+}, while Fe^{3+} can be reduced back to Fe^{2+} in the presence of additional peroxide [85]. However, beyond their formation, these radicals are also consumed through both desired reactions (oxidation of the target pollutants) and undesired side reactions. In particular, it is well documented that excess H_2O_2 and excess ferrous ion can act as scavengers of •OH, consuming these radicals before they react with the contaminants [86]. For example, hydroxyl radicals can react rapidly with H_2O_2 (when present in excess) to generate hydroperoxyl radicals (HO_2•), which are significantly less oxidizing. Similarly, excess Fe^{2+} reacts instantaneously with •OH to yield Fe^{3+}, thereby removing useful radicals from the system [87]. These competing radical pathways explain the existence of the optimal conditions observed in this study: at appropriate reagent ratios, •OH production predominates over its non-productive consumption, whereas beyond a certain point, increasing H_2O_2 or Fe^{2+} mainly intensifies parasitic radical self-consumption reactions rather than enhancing pollutant oxidation [88].

On this basis, the significant quadratic effect of the Fenton ratio observed in the results can be attributed to a balance between radical generation and radical consumption. At low $[H_2O_2]$:$[Fe^{2+}]$ ratios (for example, relatively high Fe^{2+} and low peroxide), •OH formation may be limited by the availability of H_2O_2, and a fraction of the residual Fe^{2+} can also consume the radicals produced, competing with the target pollutants [89]. In contrast, at very high peroxide-to-iron ratios, the excess unreacted H_2O_2 behaves as an undesirable scavenger of •OH, promoting the recombination/transformation of radicals into less oxidizing species (HO_2•/O_2) instead of driving contaminant degradation [90].

Several studies have reported the existence of an optimal H_2O_2 dose in Fenton and related processes, since overdosing the oxidant leads to a decrease in efficiency due to this radical scavenging effect. Indeed, at excessively high peroxide concentrations, even a reduction in the overall oxidation rate compared with the optimum has been observed, because the •OH generated is rapidly consumed by the excess H_2O_2 to form HO_2•, which is much less reactive [91]. Likewise, an optimal concentration exists for the ferrous catalyst: moderate Fe^{2+} levels accelerate •OH production, but beyond a certain threshold, adding more iron becomes counterproductive because the radicals are increasingly scavenged by the excess Fe^{2+} in solution [92]. This phenomenon has been quantified, for example, in the degradation of organic contaminants where the removal efficiency increases up to a maximum at around 1 mM Fe^{2+} and then declines as the iron dose is further increased, due to the non-productive consumption of •OH by excess Fe^{2+}. In summary, there is an optimal H_2O_2/Fe^{2+} ratio at which the generation of oxidizing radicals is maximized relative to their self-loss; beyond this point, efficiency decreases because any additional reagent mainly enhances radical self-annihilation pathways rather than useful oxidation [93].

A similar trend explains the existence of an optimum treatment time. In the early stages of the reaction, the initial concentrations of H_2O_2 and Fe^{2+} favor abundant •OH generation, and these radicals are consumed predominantly in the oxidation of the target contaminants. As time elapses, however, the reagents are progressively depleted and radical production tends to slow down. Residual H_2O_2 decreases both through its reaction with Fe^{2+} and through non-catalytic decomposition (for instance, overall disproportionation of peroxide into water and oxygen). Even in the presence of contaminants, a fraction of H_2O_2 is inevitably diverted toward dismutation into O_2 and H_2O (a waste reaction) instead of forming additional •OH. At the same time, most of the initial Fe^{2+} has been converted to Fe^{3+}, leaving the system with diminished capacity to sustain radical generation [94]. Under these conditions, the few •OH radicals formed at late stages have a much higher probability of recombining with each other or being scavenged by intermediate by-products and residual species (such as HO_2•, formed from peroxide) rather than oxidizing contaminant molecules. As a result, beyond a certain optimal reaction time, additional contaminant removal becomes marginal. Moreover, prolonging the treatment beyond this point can lead to apparently lower efficiencies, because radicals continue to be consumed in secondary reactions (and some intermediates may stabilize or recombine) without achieving substantially higher mineralization of the original pollutants. This time-dependent quadratic behavior—characterized by a maximum followed by a decline—is consistent with the typical kinetics of Fenton-based and other advanced oxidation processes [95].

It is worth noting that this pattern of optimal conditions followed by a decrease in efficiency is not exclusive to the Fenton system. It is also observed in other radical-based advanced oxidation processes. For instance, in UV/H_2O_2 photo-oxidation, an optimal peroxide dose has been reported beyond which additional •OH generation is counterbalanced by radical self-scavenging by the excess H_2O_2 [91]. Similarly, in processes that generate sulfate radicals (SO_4^{-}•) from persulfate, it has been found that adding oxidant in excess inhibits degradation efficiency because surplus persulfate scavenges SO_4^{-}• radicals and promotes their mutual recombination [96]. These analogies with other advanced oxidation systems support the mechanistic interpretation: any oxidation route mediated by highly reactive radicals tends to exhibit an optimal operating point, beyond which the generated radicals start to self-destruct or are consumed by undesired agents (including the oxidant itself), thereby reducing the overall process efficiency. Incorporating this mechanistic perspective into the discussion helps to substantiate why efficiency maxima are observed at intermediate Fenton ratios and reaction times, followed by a decline when these optima are exceeded due to radical-limited conditions caused by self-scavenging.

Figure 5 shows the photo-Fenton degradation mechanism for atrazine (ATZ) and methomyl (MET). UV irradiation (hν) accelerates the Fenton reaction (Fe^{2+}/H_2O_2) by generating highly oxidizing hydroxyl radicals (•OH). These radicals attack the contaminant molecules, leading to their oxidation and fragmentation [97]. In the case of atrazine (a triazine herbicide), •OH can dechlorinate and dealkylate the molecule, forming byproducts such as hydroxyatrazine (replacement of Cl by OH) and the degraded amines desethylatrazine (DEA) and desisopropylatrazine (DIA) [98]. Studies report that such metabolites are common in the degradation of atrazine, whether by chemical or biological pathways, with some retaining a toxicity comparable to the original atrazine (DIA, DEA), while others, such as hydroxyatrazine, are less toxic [99]. With sufficient oxidant and irradiation time, the triazine ring can be completely oxidized to cyanuric acid (trihydroxylated triazine) as a stable end product, and eventually mineralized to CO_2, H_2O, nitrates, and inorganic chlorides [100]. In fact, under intensive photo-Fenton conditions ($UV/H_2O_2/Fe$), almost complete mineralization of atrazine is possible.

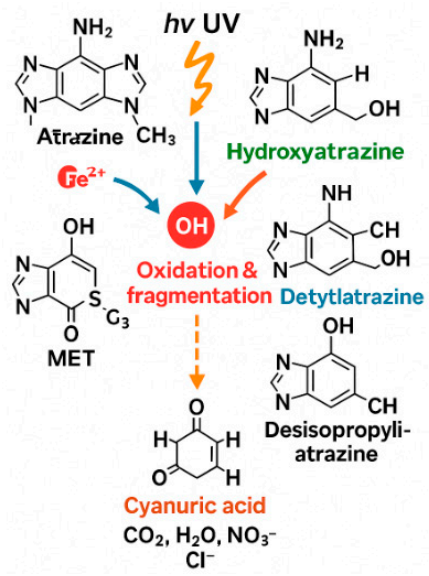


Figure 5. Proposed schematic of the photo-Fenton degradation mechanism for atrazine (ATZ) and methomyl (MET). UV irradiation (hν) accelerates the Fenton reaction (Fe^{2+}/H_2O_2), generating highly oxidative hydroxyl radicals (•OH).

Methomyl (a carbamate insecticide) undergoes a similar attack by •OH radicals. First, the sulfur atom of methomyl is oxidized to form methomyl sulfoxide (an intermediate where S is oxidized to S=O) [101]. Subsequently, hydroxyl radicals break the bonds of the molecule, generating simpler compounds. Among the end products identified for methomyl in advanced oxidation processes are acetic acid ($C_2H_4O_2$) and methanesulfonic acid (CH_3SO_3H), along with other inorganic species (e.g., CO_2, H_2O, sulfates, nitrates) [102]. These results are consistent with previous studies showing the effectiveness of photo-Fenton in completely degrading methomyl in acidic aqueous media, even surpassing the dark Fenton reaction in speed and degree of mineralization. The diagram illustrates the simplified structures of MET and its sulfoxide, indicating their subsequent conversion to small molecules and finally to harmless minerals.

4.5. Reproducibility of Optimized Conditions

To ensure reproducibility of the optimized conditions, each experimental run at the predicted optimum (flow rate = 0.466 L min^{-1}, Fenton ratio = 12.713 mg mg^{-1}, and treatment time = 71.032 min) was performed in triplicate under strictly controlled parameters of

temperature (25 ± 1 °C), pH (maintained at 3.0 ± 0.1), and irradiance (8.26 mW cm^{-2}). Prior to each run, all reagents were freshly prepared and the UV lamp intensity was calibrated using a radiometer to minimize variability in photon flux. The resulting COD removals (94.20 ± 0.04%) showed a coefficient of variation below 0.05%, demonstrating excellent reproducibility and validating the model's predictive accuracy. Moreover, the inclusion of six central replicates in the Central Composite Design (CCD) provided an internal statistical estimate of pure error and confirmed process stability (standard deviation = 0.254%, CV = 0.2736%). This procedure follows best practices reported in high-impact studies on photo-Fenton reproducibility, where replicates and calibration of irradiation intensity are recommended to ensure consistency across runs [103]. In addition, the experimental error was evaluated through lack-of-fit and ANOVA analyses, confirming that residual variability (1.86%) arises from random noise rather than systematic bias. Collectively, these steps ensure that the optimized operational conditions can be reliably reproduced under the same laboratory settings and serve as a robust basis for scale-up verification.

Although the present study primarily focused on optimizing COD and TOC removal, residual toxicity and degradation by-products are critical aspects that define the environmental viability of the photo-Fenton process. It is well documented that during the oxidation of pesticides such as atrazine and methomyl, intermediate compounds can transiently increase toxicity before complete mineralization is achieved [41]. Typical intermediates include hydroxyatrazine, desethylatrazine (DEA), and desisopropylatrazine (DIA) from atrazine degradation, as well as methomyl sulfoxide and acetamide derivatives from methomyl oxidation, some of which retain moderate toxicity [104]. However, several high-impact studies have demonstrated that when the process is operated under optimized photo-Fenton conditions—ensuring sufficient radical availability and treatment time—the concentration of these intermediates is significantly reduced, and the final effluent exhibits minimal or no acute toxicity. For example, [105] reported complete elimination of Daphnia magna toxicity after 30 min of post-treatment with Fenton/photo-Fenton, despite the initial presence of multiple pesticide by-products. Similarly, [38] observed a 90% reduction in toxicity units (TU) alongside >79% DOC removal when treating real pesticide-contaminated effluents via solar photo-Fenton, confirming the detoxification capacity of the process at advanced mineralization levels.

In the present study, the optimized photo-Fenton conditions achieved high mineralization (81% TOC removal), suggesting that most organic intermediates were converted into low-toxicity species such as carboxylic acids, nitrates, sulfates, and chlorides, as previously reported in advanced oxidation literature [100]. Therefore, given the high degree of mineralization achieved here, the residual toxicity is expected to be minimal. Nevertheless, future work will include ecotoxicity assays to confirm the complete detoxification of the treated effluent and to characterize any trace by-products using LC–MS/MS, following recommendations from recent studies on pesticide degradation pathways [99]. Collectively, evidence from the literature and the high mineralization efficiency achieved in this work indicate that the optimized photo-Fenton system not only ensures substantial removal of organic load but also promotes detoxification of the effluent, supporting its environmental feasibility for sustainable wastewater treatment applications.

4.6. Limitations and Practical Implications

While the optimized conditions (flow rate = 0.466 L min^{-1}, Fenton ratio = 12.713 mg/L, treatment time = 71.032 min) yield high COD removal in laboratory-scale tests, the practical implementation at full scale must carefully consider the high reagent demand and associated costs. It is well documented that classical and photo-Fenton processes suffer from limitations related to excessive chemical consumption, reagent instability, and generation

of iron sludge, which can compromise economic viability and environmental acceptability in real-world wastewater treatment scenarios [106].

Moreover, scaling up such optimized conditions would likely increase operational costs and reagent usage per volume treated, given that hydrogen peroxide (and iron salts) constitute significant recurring expenses. A recent critical review on Fenton/photo-Fenton applications emphasizes that, although the process is highly effective for organic pollutant degradation, its sustainability is constrained by reagent consumption, sludge management, and pH adjustments, particularly for high-volume or continuous-flow industrial effluents [107].

Therefore, while the results are promising at bench scale, translating them to real wastewater treatment would require additional measures:

- Optimization of reagent dosages and recovery/reuse of iron (to reduce sludge and costs).
- Economic and life-cycle analysis (reactant cost, sludge disposal, energy for mixing/flow).
- Pilot-scale tests under real effluent conditions (variable flow, pollutant load, matrix complexity).

In sum, the optimized conditions are suitable to demonstrate the maximum treatment potential under controlled conditions. However, for real-world applications, a follow-up study focusing on cost–benefit, reagent recycling, and process scaling is necessary to ensure sustainability and feasibility.

5. Conclusions

The present study demonstrated that the photo-Fenton process is a highly effective alternative for the simultaneous degradation of atrazine and methomyl in aqueous solution, achieving advanced levels of mineralization. Based on a 2^3 factorial design, the H_2O_2/Fe^{2+} ratio was identified as the predominant factor influencing chemical oxygen demand (COD) removal, while irradiation time exhibited a secondary positive effect and volumetric flow rate showed only marginal influence. The sequential application of central points and the path of steepest ascent allowed approximation to the region of highest efficiency, where the Central Composite Design–RSM revealed significant curvature of the response surface. The resulting quadratic model explained 98.14% of the experimental variability ($R^2 = 0.9814$) and exhibited satisfactory predictive capacity (R^2_pred = 0.8591), with a residual coefficient of variation of 0.27%, reflecting the precision and reproducibility of the system.

The integration of Response Surface Methodology (RSM) and the homogeneous photo-Fenton process demonstrated a powerful and reproducible strategy for optimizing the simultaneous degradation of multiple pesticides under realistic agricultural effluent conditions. The optimized configuration—defined by a volumetric flow rate of 0.466 L min^{-1}, a Fenton ratio of 12.713 mg mg^{-1}, and a treatment time of 71 min—achieved 94.5% COD and 81% TOC removal, outperforming conventional photo-Fenton or TiO_2-based photocatalytic systems in both mineralization and energy efficiency. These results are consistent with previous RSM-driven optimizations that reported over 90% pollutant abatement in textile and refinery wastewaters under statistically tuned operational parameters. Furthermore, the model's predictive robustness ($R^2 = 0.9814$; R^2_pred = 0.8591) confirms the reliability of RSM for scaling and transferring laboratory conditions to pilot systems, as similarly validated in petrochemical and food-processing wastewater applications. Therefore, the optimized homogeneous photo-Fenton process provides a statistically validated, energy-efficient, and scalable solution for the treatment of mixed-pesticide wastewaters, aligning with global efforts toward sustainable and circular water management in agriculture.

Author Contributions: Conceptualization, L.B.-T. and A.P.-N.; methodology, C.C.-S., P.V.-V., A.M.-F., A.V.-R. and J.M.d.l.C.; software, C.R.-V.d.O. and A.V.-R.; validation, J.M.d.l.C. and L.O.-G.; formal analysis, C.R.-V.d.O. and A.V.-R.; investigation, C.C.-S., P.V.-V., A.M.-F., L.B.-T., M.B.-N. and L.O.-G.; resources, A.P.-N.; data curation, L.O.-G.; writing—original draft preparation, N.C.-C. and L.O.-G.; writing—review and editing, all authors; visualization, J.M.d.l.C. and N.C.-C.; supervision, A.P.-N., M.B.-N. and C.C.-S.; project administration, L.B.-T. and A.P.-N. All authors have read and agreed to the published version of the manuscript.

Funding: This research received no external funding.

Institutional Review Board Statement: Not applicable.

Informed Consent Statement: Not applicable.

Data Availability Statement: The original contributions presented in the study are included in the article, further inquiries can be directed to the corresponding author.

Conflicts of Interest: The authors declare no conflicts of interest.

Abbreviations

The following abbreviations are used in this manuscript:

AOP	Advanced Oxidation Process
ATZ	Atrazine
CCD	Central Composite Design
COD	Chemical Oxygen Demand
CV	Coefficient of Variation
MET	Methomyl
•OH	Hydroxyl Radical
PRESS	Predicted Residual Error Sum of Squares
RSM	Response Surface Methodology

References

1. Morin-Crini, N.; Lichtfouse, E.; Liu, G.; Balaram, V.; Ribeiro, A.R.L.; Lu, Z.; Stock, F.; Carmona, E.; Teixeira, M.R.; Picos-Corrales, L.A. Worldwide cases of water pollution by emerging contaminants: A review. *Environ. Chem. Lett.* **2022**, *20*, 2311–2338. [CrossRef]
2. Almeida-Naranjo, C.E.; Guerrero, V.H.; Villamar-Ayala, C.A. Emerging contaminants and their removal from aqueous media using conventional/non-conventional adsorbents: A glance at the relationship between materials, processes, and technologies. *Water* **2023**, *15*, 1626. [CrossRef]
3. Ritter, L.; Solomon, K.; Sibley, P.; Hall, K.; Keen, P.; Mattu, G.; Linton, B. Sources, pathways, and relative risks of contaminants in surface water and groundwater: A perspective prepared for the Walkerton inquiry. *J. Toxicol. Environ. Health Part A* **2002**, *65*, 1–142.
4. Riaz, U.; Rafi, F.; Naveed, M.; Mehdi, S.M.; Murtaza, G.; Niazi, A.G.; Mehmood, H. Pesticide pollution in an aquatic environment. In *Freshwater Pollution and Aquatic Ecosystems*; Apple Academic Press: Point Pleasant, NJ, USA, 2021; pp. 131–163.
5. Singh, S.; Kumar, V.; Chauhan, A.; Datta, S.; Wani, A.B.; Singh, N.; Singh, J. Toxicity, degradation and analysis of the herbicide atrazine. *Environ. Chem. Lett.* **2018**, *16*, 211–237. [CrossRef]
6. Struger, J.; Grabuski, J.; Cagampan, S.; Sverko, E.; Marvin, C. Occurrence and distribution of carbamate pesticides and metalaxyl in southern Ontario surface waters 2007–2010. *Bull. Environ. Contam. Toxicol.* **2016**, *96*, 423–431. [CrossRef]
7. Hong, J.; Boussetta, N.; Enderlin, G.; Merlier, F.; Grimi, N. Degradation of residual herbicide atrazine in agri-food and washing water. *Foods* **2022**, *11*, 2416. [CrossRef]
8. Lin, Z.; Zhang, W.; Pang, S.; Huang, Y.; Mishra, S.; Bhatt, P.; Chen, S. Current approaches to and future perspectives on methomyl degradation in contaminated soil/water environments. *Molecules* **2020**, *25*, 738. [CrossRef]
9. Sharma, N.; Yadav, A.; Yadav, S.; Panghal, P.; Singh, S.; Deep, A.; Kumar, S. Biomass-based adsorbents for wastewater remediation: A systematic review on removal of emerging contaminants. *Microchem. J.* **2024**, *207*, 111880. [CrossRef]
10. Yadav, D.; Rangabhashiyam, S.; Verma, P.; Singh, P.; Devi, P.; Kumar, P.; Hussain, C.M.; Gaurav, G.K.; Kumar, K.S. Environmental and health impacts of contaminants of emerging concerns: Recent treatment challenges and approaches. *Chemosphere* **2021**, *272*, 129492. [CrossRef]

11. Zhao, H.; Qian, H.; Cui, J.; Ge, Z.; Shi, J.; Huo, Y.; Zhang, Y.; Ye, L. Endocrine toxicity of atrazine and its underlying mechanisms. *Toxicology* **2024**, *505*, 153846. [CrossRef]
12. Gonsioroski, A.; Mourikes, V.E.; Flaws, J.A. Endocrine disruptors in water and their effects on the reproductive system. *Int. J. Mol. Sci.* **2020**, *21*, 1929. [CrossRef] [PubMed]
13. Jablonski, C.A.; Pereira, T.C.B.; Teodoro, L.D.S.; Altenhofen, S.; Rübensam, G.; Bonan, C.D.; Bogo, M.R. Acute toxicity of methomyl commercial formulation induces morphological and behavioral changes in larval zebrafish (Danio rerio). *Neurotoxicol. Teratol.* **2022**, *89*, 107058. [CrossRef] [PubMed]
14. Alharbi, F.K. Effect of Methomyl on Fetal Development in Female Rats. *Egypt. J. Chem. Environ. Health* **2018**, *4*, 32–42. [CrossRef]
15. Mörtl, M.; Kereki, O.; Darvas, B.; Klátyik, S.; Vehovszky, Á.; Győri, J.; Székács, A. Study on soil mobility of two neonicotinoid insecticides. *J. Chem.* **2016**, *2016*, 4546584. [CrossRef]
16. Li, Y.; Li, Y.; Bi, G.; Ward, T.J.; Li, L. Adsorption and degradation of neonicotinoid insecticides in agricultural soils. *Environ. Sci. Pollut. Res.* **2023**, *30*, 47516–47526. [CrossRef]
17. Todey, S.A.; Fallon, A.M.; Arnold, W.A. Neonicotinoid insecticide hydrolysis and photolysis: Rates and residual toxicity. *Environ. Toxicol. Chem.* **2018**, *37*, 2797–2809. [CrossRef]
18. Mokhtar, H.I.; Abdel-Latif, H.A.; ElMazoudy, R.H.; Abdelwahab, W.M.; Saad, M.I. Effect of methomyl on fertility, embryotoxicity and physiological parameters in female rats. *J. Appl. Pharm. Sci.* **2013**, *3*, 109–119.
19. Liang, C.-A.; Chang, S.-S.; Chen, H.-Y.; Tsai, K.-F.; Lee, W.-C.; Wang, I.-K.; Chen, C.-Y.; Liu, S.-H.; Weng, C.-H.; Huang, W.-H. Human poisoning with methomyl and cypermethrin pesticide mixture. *Toxics* **2023**, *11*, 372. [CrossRef]
20. de Figueiredo Neves, T.; Camparotto, N.G.; de Vargas Brião, G.; Mastelaro, V.R.; Vieira, M.G.A.; Dantas, R.F.; Prediger, P. Synergetic effect on the adsorption of cationic and anionic emerging contaminants on polymeric membranes containing Modified-Graphene Oxide: Study of mechanism in binary systems. *J. Mol. Liq.* **2023**, *383*, 122045. [CrossRef]
21. Shanmugavel, S.P.; Kumar, G. Recent progress in mineralization of emerging contaminants by advanced oxidation process: A review. *Environ. Pollut.* **2024**, *341*, 122842.
22. Qu, S.; Wang, R.; Wei, M.; Hu, X.; Song, X. Advanced oxidation processes mediated by Schwertmannite for the degradation of organic emerging contaminants: Mechanism and synergistic approach. *J. Water Process Eng.* **2024**, *68*, 106527. [CrossRef]
23. Chen, K.; Huang, X.; Zhu, G.; Pang, H.; Lu, J.; Zhang, Z. Unraveling the triple mechanisms of advanced coagulation for removal of emerging and conventional contaminants: Oxidation, hydrolytic coagulation and surface hydroxylation adsorption. *Chem. Eng. J.* **2024**, *484*, 149473. [CrossRef]
24. Mousavi, S.L.; Sajjadi, S.M. Predicting rejection of emerging contaminants through RO membrane filtration based on ANN-QSAR modeling approach: Trends in molecular descriptors and structures towards rejections. *RSC Adv.* **2023**, *13*, 23754–23771. [CrossRef] [PubMed]
25. Chen, R.; Zhang, H.; Wang, J.; Xu, D.; Tang, X.; Gong, W.; Liang, H. Insight into the role of biogenic manganese oxides-assisted gravity-driven membrane filtration systems toward emerging contaminants removal. *Water Res.* **2022**, *224*, 119111. [CrossRef]
26. Chen, R.; Hu, L.; Zhang, H.; Lin, D.; Wang, J.; Xu, D.; Gong, W.; Liang, H. Toward emerging contaminants removal using acclimated activated sludge in the gravity-driven membrane filtration system. *J. Hazard. Mater.* **2022**, *438*, 129541. [CrossRef]
27. Shao, D.; Zhang, B.; Zhao, W.; Feng, J.; Xu, H.; Zhu, C.; Yan, W.; Jia, X.; Song, H. Enhanced removal of aromatic emerging contaminants through the electrochemical co-degradation with polystyrene microplastics. *Chem. Eng. J.* **2025**, *509*, 161535. [CrossRef]
28. Xue, W.; Tabucanon, A.S.; Amarakoon, A.M.S.N.; Xiao, K.; Huang, X. Recent advances in membrane and electrochemical hybrid technologies for emerging contaminants removal. *Water Cycle* **2025**, *6*, 176–194. [CrossRef]
29. Codina, A.S.; Lumbaque, E.C.; Radjenovic, J. Electrochemical removal of contaminants of emerging concern with manganese oxide-functionalized graphene sponge electrode. *Chem. Eng. J.* **2025**, *508*, 160940. [CrossRef]
30. Tian, M.; Chang, J.; Ding, J.; Yin, Y. Impact of coexisting components on the catalytic ozonation of emerging contaminants in wastewater. *Sep. Purif. Technol.* **2025**, *362*, 131847. [CrossRef]
31. Guo, Y.; Zhu, S.; Wang, B.; Huang, J.; Deng, S.; Yu, G.; Wang, Y. Modelling of emerging contaminant removal during heterogeneous catalytic ozonation using chemical kinetic approaches. *J. Hazard. Mater.* **2019**, *380*, 120888. [CrossRef]
32. Wang, J.; Bai, Z. Fe-based catalysts for heterogeneous catalytic ozonation of emerging contaminants in water and wastewater. *Chem. Eng. J.* **2017**, *312*, 79–98. [CrossRef]
33. Wang, C.; Li, Y.; Wang, Z.; Lei, J.; Sun, S.-P. High-valent ferryl intermediates generation, reactivity and kinetic characterization with contaminants of emerging concern via a facile photo-Fenton competition kinetic methodology. *J. Hazard. Mater.* **2025**, *492*, 138216. [CrossRef] [PubMed]
34. Júnior, F.E.B.; Marin, B.T.; Mira, L.; Fernandes, C.H.M.; Fortunato, G.V.; Almeida, M.O.; Honório, K.M.; Colombo, R.; de Siervo, A.; Lanza, M.R.V.; et al. Monitoring Photo-Fenton and Photo-Electro-Fenton process of contaminants emerging concern by a gas diffusion electrode using $Ca_{10-x}Fe_{x-y}W_y(PO_4)_6(OH)_2$ nanoparticles as heterogeneous catalyst. *Chemosphere* **2024**, *361*, 142515. [CrossRef] [PubMed]

35. Campos, S.; Lorca, J.; Vidal, J.; Calzadilla, W.; Toledo-Neira, C.; Aranda, M.; Miralles-Cuevas, S.; Cabrera-Reina, A.; Salazar, R. Removal of contaminants of emerging concern by solar photo electro-Fenton process in a solar electrochemical raceway pond reactor. *Process Saf. Environ. Prot.* **2023**, *169*, 660–670. [CrossRef]
36. Silva, M.; Baltrus, J.P.; Williams, C.; Knopf, A.; Zhang, L.; Baltrusaitis, J. Heterogeneous photo-Fenton-like degradation of emerging pharmaceutical contaminants in wastewater using Cu-doped MgO nanoparticles. *Appl. Catal. A Gen.* **2022**, *630*, 118468. [CrossRef]
37. Fareed, A.; Hussain, A.; Nawaz, M.; Imran, M.; Ali, Z.; Haq, S.U. The impact of prolonged use and oxidative degradation of Atrazine by Fenton and photo-Fenton processes. *Environ. Technol. Innov.* **2021**, *24*, 101840. [CrossRef]
38. Gomes Júnior, O.; Santos, M.G.B.; Nossol, A.B.S.; Starling, M.C.V.M.; Trovó, A.G. Decontamination and toxicity removal of an industrial effluent containing pesticides via multistage treatment: Coagulation-flocculation-settling and photo-Fenton process. *Process Saf. Environ. Prot.* **2021**, *147*, 674–683. [CrossRef]
39. Sanabria Florez, P.L.; Los Weinert, P.; Lopes Tiburtius, E.R. Assessment of UV-Vis LED-assisted Photo-Fenton Reactor for Atrazine Degradation in Aqueous Solution. *Orbital Electron. J. Chem.* **2021**, *13*, 160–169.
40. Zhang, H.-M.; Cheng, S.-T.; Shen, X.-F.; Pang, Y.-H. Bimetallic MOF sulfurized In2S3/Fe3S4 for efficient photo-Fenton degradation of atrazine under weak sunlight: Mechanism insight and degradation pathways. *J. Water Process Eng.* **2024**, *68*, 106520. [CrossRef]
41. Rodrigues-Silva, F.; Masceno, G.P.; Panicio, P.P.; Imoski, R.; Prola, L.D.T.; Vidal, C.B.; Xavier, C.R.; Ramsdorf, W.A.; Passig, F.H.; de Liz, M.V. Removal of micropollutants by UASB reactor and post-treatment by Fenton and photo-Fenton: Matrix effect and toxicity responses. *Environ. Res.* **2022**, *212*, 113396. [CrossRef]
42. Hayat, W.; Zhang, Y.; Huang, S.; Hussain, I.; Huang, R. Insight into the degradation of methomyl in water by peroxymonosulfate. *J. Environ. Chem. Eng.* **2021**, *9*, 105358. [CrossRef]
43. Mohammed, N.A.; Alwared, A.I.; Shakhir, K.S.; Sulaiman, F.A. Synthesis, characterization of $FeNi_3$@ SiO_2@ CuS for enhance solar photocatalytic degradation of atrazine herbicides: Application of RSM. *Results Surf. Interfaces* **2024**, *16*, 100253. [CrossRef]
44. El-Gawad, H.A.; Ghaly, M.Y.; El Hussieny, N.F.; Abdel Kreem, M.; Reda, Y. Novel collector design and optimized photo-fenton model for sustainable industry textile wastewater treatment. *Sci. Rep.* **2024**, *14*, 8573. [CrossRef] [PubMed]
45. Martín, M.; Pérez, J.; López, J.; Oller, I.; Rodríguez, S. Degradation of a four-pesticide mixture by combined photo-Fenton and biological oxidation. *Water Res.* **2009**, *43*, 653–660. [CrossRef]
46. Abdessalem, A.; Bellakhal, N.; Oturan, N.; Dachraoui, M.; Oturan, M. Treatment of a mixture of three pesticides by photo- and electro-Fenton processes. *Desalination* **2010**, *250*, 450–455. [CrossRef]
47. Zekkaoui, C.; Berrama, T.; Dumoulin, D.; Billon, G.; Kadmi, Y. Optimal degradation of organophosphorus pesticide at low levels in water using fenton and photo-fenton processes and identification of by-products by GC-MS/MS. *Chemosphere* **2021**, *279*, 130544. [CrossRef]
48. Schenone, A.V.; Conte, L.O.; Botta, M.A.; Alfano, O.M. Modeling and optimization of photo-Fenton degradation of 2, 4-D using ferrioxalate complex and response surface methodology (RSM). *J. Environ. Manag.* **2015**, *155*, 177–183. [CrossRef]
49. Rad, L.R.; Irani, M.; Pourahmad, H.; Sayyafan, M.S.; Haririan, I. Simultaneous degradation of phenol and paracetamol during photo-Fenton process: Design and optimization. *J. Taiwan Inst. Chem. Eng.* **2015**, *47*, 190–196. [CrossRef]
50. Calza, P.; Sakkas, V.A.; Medana, C.; Vlachou, A.D.; Dal Bello, F.; Albanis, T.A. Chemometric assessment and investigation of mechanism involved in photo-Fenton and TiO_2 photocatalytic degradation of the artificial sweetener sucralose in aqueous media. *Appl. Catal. B Environ.* **2013**, *129*, 71–79. [CrossRef]
51. Tamimi, M.; Qourzal, S.; Barka, N.; Assabbane, A.; Ait-Ichou, Y. Methomyl degradation in aqueous solutions by Fenton's reagent and the photo-Fenton system. *Sep. Purif. Technol.* **2008**, *61*, 103–108. [CrossRef]
52. Popova, S.; Tsenter, I.; Garkusheva, N.; Beck, S.E.; Matafonova, G.; Batoev, V. Evaluating (sono)-photo-Fenton-like processes with high-frequency ultrasound and UVA LEDs for degradation of organic micropollutants and inactivation of bacteria separately and simultaneously. *J. Environ. Chem. Eng.* **2021**, *9*, 105249. [CrossRef]
53. Khan, J.A.; He, X.; Khan, H.M.; Shah, N.S.; Dionysiou, D.D. Oxidative degradation of atrazine in aqueous solution by $UV/H_2O_2/Fe^{2+}$, $UV/S2O_8^{2-}/Fe^{2+}$ and $UV/HSO_5^{-}/Fe^{2+}$ processes: A comparative study. *Chem. Eng. J.* **2013**, *218*, 376–383. [CrossRef]
54. Xu, S.; Wu, D.; Hu, Z. Impact of hydraulic retention time on organic and nutrient removal in a membrane coupled sequencing batch reactor. *Water Res.* **2014**, *55*, 12–20. [CrossRef] [PubMed]
55. Al-Shannag, M.; Lafi, W.; Bani-Melhem, K.; Gharagheer, F.; Dhaimat, O. Reduction of COD and TSS from paper industries wastewater using electro-coagulation and chemical coagulation. *Sep. Sci. Technol.* **2012**, *47*, 700–708. [CrossRef]
56. Frost, J. Multiple regression analysis: Use adjusted R-squared and predicted R-squared to include the correct number of variables. *Minitab Blog* **2013**, *13*. Available online: https://blog.minitab.com/en/blog/adventures-in-statistics-2/multiple-regression-analysis-use-adjusted-r-squared-and-predicted-r-squared-to-include-the-correct-number-of-variables (accessed on 4 January 2026).
57. Frost, J. How to interpret adjusted R-squared and predicted R-squared in regression analysis. *Retrieved Oktober* **2019**, *25*, 2019.

58. Siraj, E.A.; Mulualem, Y.; Molla, F.; Yayehrad, A.T.; Belete, A. Formulation optimization of furosemide floating-bioadhesive matrix tablets using waste-derived Citrus aurantifolia peel pectin as a polymer. *Sci. Rep.* **2025**, *15*, 16704. [CrossRef]
59. Hiralal Dhage, B.; Khedkar, N.K. Predictive machine learning and printing parameter optimization for enhanced impact performance of 3D-printed Onyx-Kevlar composites. *Discov. Mater.* **2025**, *5*, 174. [CrossRef]
60. Zambom, A.Z.; Akritas, M.G. NonpModelCheck: An R package for nonparametric lack-of-fit testing and variable selection. *J. Stat. Softw.* **2017**, *77*, 1–28. [CrossRef]
61. Khoshraftar, Z. Modeling of CO_2 solubility and partial pressure in blended diisopropanolamine and 2-amino-2-methylpropanol solutions via response surface methodology and artificial neural network. *Sci. Rep.* **2025**, *15*, 1800. [CrossRef]
62. Myśliwiec, P.; Szawara, P.; Kubit, A.; Zwolak, M.; Ostrowski, R.; Derazkola, H.A.; Jurczak, W. FSW optimization: Prediction using polynomial regression and optimization with hill-climbing method. *Materials* **2025**, *18*, 448. [CrossRef]
63. Aerts, M.; Claeskens, G.; Hart, J.D. Testing lack of fit in multiple regression. *Biometrika* **2000**, *87*, 405–424. [CrossRef]
64. Kang, J.-K.; Lee, Y.-J.; Son, C.-Y.; Park, S.-J.; Lee, C.-G. Alternative assessment of machine learning to polynomial regression in response surface methodology for predicting decolorization efficiency in textile wastewater treatment. *Chemosphere* **2025**, *370*, 143996. [CrossRef] [PubMed]
65. Montesinos López, O.A.; Montesinos López, A.; Crossa, J. Overfitting, Model Tuning, and Evaluation of Prediction Performance. In *Multivariate Statistical Machine Learning Methods for Genomic Prediction*; Springer: Cham, Switzerland, 2022; pp. 109–139.
66. Shah, M.I.; Abunama, T.; Javed, M.F.; Bux, F.; Aldrees, A.; Tariq, M.A.U.R.; Mosavi, A. Modeling surface water quality using the adaptive neuro-fuzzy inference system aided by input optimization. *Sustainability* **2021**, *13*, 4576. [CrossRef]
67. Irfan, M.F.; Hossain, Z.; Ans, M.; Al-Anzil, B.S.; Ullah, A. Implementation of statistical response surface methodology with desirability function for ion-exchange-based selective demineralization of municipal wastewater and tap water for drinking purposes. *Int. J. Environ. Sci. Technol.* **2025**, *22*, 7753–7768. [CrossRef]
68. Ray, D.K.; Gerber, J.S.; MacDonald, G.K.; West, P.C. Climate variation explains a third of global crop yield variability. *Nat. Commun.* **2015**, *6*, 5989. [CrossRef]
69. Santos Nobre, J.; da Motta Singer, J. Residual analysis for linear mixed models. *Biom. J. J. Math. Methods Biosci.* **2007**, *49*, 863–875.
70. Rizopoulos, D.; Moustaki, I. Generalized latent variable models with non-linear effects. *Br. J. Math. Stat. Psychol.* **2008**, *61*, 415–438. [CrossRef]
71. Passerine, B.F.G.; Breitkreitz, M.C. Important Aspects of the Design of Experiments and Data Treatment in the Analytical Quality by Design Framework for Chromatographic Method Development. *Molecules* **2024**, *29*, 6057. [CrossRef]
72. Popli, D.; Gupta, M. Rotary ultrasonic machining of ni based alloys. *Int. J. Innov. Res. Sci. Technol.* **2017**, *3*, 140–151.
73. Alalm, M.G.; Tawfik, A.; Ookawara, S. Comparison of solar TiO_2 photocatalysis and solar photo-Fenton for treatment of pesticides industry wastewater: Operational conditions, kinetics, and costs. *J. Water Process Eng.* **2015**, *8*, 55–63. [CrossRef]
74. Giri, A.; Golder, A. Fenton, Photo-Fenton, H_2O_2 Photolysis, and TiO_2 Photocatalysis for Dipyrone Oxidation: Drug Removal, Mineralization, Biodegradability, and Degradation Mechanism. *Ind. Eng. Chem. Res.* **2014**, *53*, 1351–1358. [CrossRef]
75. Aljubourya, D.; Palaniandy, P.; Aziz, H.; Feroz, S. Comparative Study to the Solar Photo-Fenton, Solar Photocatalyst of TiO_2 and Solar Photocatalyst of TiO_2 Combined with Fenton Process to Treat Petroleum Wastewater by RSM. *J. Pet. Environ. Biotechnol.* **2016**, *7*, 2.
76. Martini, S.; Afroze, S.; Roni, K. Raw Industrial Wastewater Treatment Using Fenton, Photo Fenton and Photo Catalytic: A Comparison Study. In *IOP Conference Series: Earth and Environmental Science*; IOP Publishing: Bristol, UK, 2021; Volume 801.
77. Gernjak, W.; Maldonado, M.; Malato, S.; Cáceres, J.; Krutzler, T.; Glaser, A.; Bauer, R. Pilot-plant treatment of olive mill wastewater (OMW) by solar TiO_2 photocatalysis and solar photo-Fenton. *Sol. Energy* **2004**, *77*, 567–572. [CrossRef]
78. al deen Atallah, D.; Palaniandy, P.; Aziz, H.B.A.; Feroz, S. Evaluating the TiO_2 as a solar photocatalyst process by response surface methodology to treat the petroleum waste water. *Karbala Int. J. Mod. Sci.* **2015**, *1*, 78–85. [CrossRef]
79. al deen Atallah, D.; Palaniandy, P.; Aziz, H.B.A.; Feroz, S. Treatment of petroleum wastewater using combination of solar photo-two catalyst TiO2 and photo-Fenton process. *J. Environ. Chem. Eng.* **2015**, *3*, 1117–1124.
80. Bhatti, D.T.; Parikh, S.P. Solar light induced photocatalysis for treatment of high COD pharmaceutical effluent with recyclable Ag-Fe codoped TiO_2: Kinetics of COD removal. *Curr. World Environ.* **2020**, *15*, 137. [CrossRef]
81. Wu, D.; Li, C.; Zhang, D.; Wang, L.; Zhang, X.; Shi, Z.; Lin, Q. Photocatalytic improvement of Y^{3+} modified TiO_2 prepared by a ball milling method and application in shrimp wastewater treatment. *RSC Adv.* **2019**, *9*, 14609–14620. [CrossRef]
82. Kweinor Tetteh, E.; Rathilal, S. Adsorption and photocatalytic mineralization of bromophenol blue dye with TiO_2 modified with clinoptilolite/activated carbon. *Catalysts* **2020**, *11*, 7. [CrossRef]
83. Amorós-Pérez, A.; Lillo-Ródenas, M.Á.; Román-Martínez, M.D.C.; García-Muñoz, P.; Keller, N. TiO_2 and TiO_2-carbon hybrid photocatalysts for diuron removal from water. *Catalysts* **2021**, *11*, 457. [CrossRef]
84. Speltini, A.; Maraschi, F.; Sturini, M.; Caratto, V.; Ferretti, M.; Profumo, A. Sorbents Coupled to Solar Light TiO_2-Based Photocatalysts for Olive Mill Wastewater Treatment. *Int. J. Photoenergy* **2016**, *2016*, 8793841. [CrossRef]

85. Fischbacher, A.; von Sonntag, C.; Schmidt, T.C. Hydroxyl radical yields in the Fenton process under various pH, ligand concentrations and hydrogen peroxide/Fe (II) ratios. *Chemosphere* **2017**, *182*, 738–744. [CrossRef]
86. Pignatello, J.J.; Oliveros, E.; MacKay, A. Advanced oxidation processes for organic contaminant destruction based on the Fenton reaction and related chemistry. *Crit. Rev. Environ. Sci. Technol.* **2006**, *36*, 1–84. [CrossRef]
87. Shu, Z.; Bolton, J.R.; Belosevic, M.; El Din, M.G. Photodegradation of emerging micropollutants using the medium-pressure UV/H2O2 advanced oxidation process. *Water Res.* **2013**, *47*, 2881–2889. [CrossRef] [PubMed]
88. Omar, B.M.; Zyadah, M.A.; Ali, M.Y.; El-Sonbati, M.A. Pre-treatment of composite industrial wastewater by Fenton and electro-Fenton oxidation processes. *Sci. Rep.* **2024**, *14*, 27906. [CrossRef] [PubMed]
89. Urbański, N.; Beręsewicz, A. Generation of · OH initiated by interaction of Fe2+ and Cu+ with dioxygen; comparison with the Fenton chemistry. *Acta Biochim. Pol.* **2000**, *47*, 951–962. [CrossRef] [PubMed]
90. Khan, N.A.; Khan, A.H.; Tiwari, P.; Zubair, M.; Naushad, M. New insights into the integrated application of Fenton-based oxidation processes for the treatment of pharmaceutical wastewater. *J. Water Process Eng.* **2021**, *44*, 102440. [CrossRef]
91. Rezaee, R.; Maleki, A.; Jafari, A.; Mazloomi, S.; Zandsalimi, Y.; Mahvi, A.H. Application of response surface methodology for optimization of natural organic matter degradation by UV/H_2O_2 advanced oxidation process. *J. Environ. Heal. Sci. Eng.* **2014**, *12*, 67. [CrossRef]
92. Nidheesh, P.V.; Behera, B.; Babu, D.S.; Scaria, J.; Kumar, M.S. Mixed industrial wastewater treatment by the combination of heterogeneous electro-Fenton and electrocoagulation processes. *Chemosphere* **2022**, *290*, 133348. [CrossRef]
93. Mukherjee, J.; Lodh, B.K.; Sharma, R.; Mahata, N.; Shah, M.P.; Mandal, S.; Ghanta, S.; Bhunia, B. Advanced oxidation process for the treatment of industrial wastewater: A review on strategies, mechanisms, bottlenecks and prospects. *Chemosphere* **2023**, *345*, 140473. [CrossRef]
94. Duca, G.; Travin, S. Reactions' mechanisms and applications of hydrogen peroxide. *Am. J. Phys. Chem.* **2020**, *9*, 36–44. [CrossRef]
95. Amr, S.S.A.; Aziz, H.A. New treatment of stabilized leachate by ozone/Fenton in the advanced oxidation process. *Waste Manag.* **2012**, *32*, 1693–1698. [CrossRef]
96. Norzaee, S.; Taghavi, M.; Djahed, B.; Mostafapour, F.K. Degradation of Penicillin G by heat activated persulfate in aqueous solution. *J. Environ. Manag.* **2018**, *215*, 316–323. [CrossRef]
97. Ma, J.; Ma, W.; Song, W.; Chen, C.; Tang, Y.; Zhao, J.; Huang, Y.; Xu, Y.; Zang, L. Fenton degradation of organic pollutants in the presence of low-molecular-weight organic acids: Cooperative effect of quinone and visible light. *Environ. Sci. Technol.* **2006**, *40*, 618–624. [CrossRef]
98. Pathak, R.K.; Dikshit, A.K. Atrazine and human health. *Int. J. Ecosyst.* **2011**, *1*, 14–23. [CrossRef]
99. Çokay, E. Effects of the heterogeneous photo-Fenton oxidation and sulfate radical-based oxidation on atrazine degradation. *Desalin. Water Treat.* **2022**, *252*, 233–242. [CrossRef]
100. Benzaquén, T.B.; Cuello, N.I.; Alfano, O.M.; Eimer, G.A. Degradation of Atrazine over a heterogeneous photo-fenton process with iron modified MCM-41 materials. *Catal. Today* **2017**, *296*, 51–58. [CrossRef]
101. Van Scoy, A.R.; Yue, M.; Deng, X.; Tjeerdema, R.S. Environmental fate and toxicology of methomyl. *Rev. Environ. Contam. Toxicol.* **2012**, *222*, 93–109.
102. Chang, C.-C.; Trinh, C.; Chiu, C.-Y.; Chang, C.-Y.; Chiang, S.-W.; Ji, D.-R.; Tseng, J.-Y.; Chang, C.-F.; Chen, Y.-H. UV-C irradiation enhanced ozonation for the treatment of hazardous insecticide methomyl. *J. Taiwan Inst. Chem. Eng.* **2015**, *49*, 100–104. [CrossRef]
103. Wang, R.; Li, J.; Jiang, Y.; Lu, Z.; Li, R.; Li, J. Heterologous expression of mlrA gene originated from Novosphingobium sp. THN1 to degrade microcystin-RR and identify the first step involved in degradation pathway. *Chemosphere* **2017**, *184*, 159–167. [CrossRef]
104. Adam-Guillermin, C.; Pereira, S.; Della-Vedova, C.; Hinton, T.; Garnier-Laplace, J. Genotoxic and reprotoxic effects of tritium and external gamma irradiation on aquatic animals. *Rev. Environ. Contam. Toxicol.* **2012**, *220*, 67–103.
105. Rodrigues-Silva, F.; Lemos, C.R.; Naico, A.A.; Fachi, M.M.; do Amaral, B.; de Paula, V.C.S.; Rampon, D.S.; Beraldi-Magalhães, F.; Prola, L.D.T.; Pontarolo, R. Study of isoniazid degradation by Fenton and photo-Fenton processes, by-products analysis and toxicity evaluation. *J. Photochem. Photobiol. A Chem.* **2022**, *425*, 113671. [CrossRef]
106. Ziembowicz, S.; Kida, M. Limitations and future directions of application of the Fenton-like process in micropollutants degradation in water and wastewater treatment: A critical review. *Chemosphere* **2022**, *296*, 134041. [CrossRef]
107. Machado, F.; Teixeira, A.; Ruotolo, L.A.M. Critical review of Fenton and photo-Fenton wastewater treatment processes over the last two decades. *Int. J. Environ. Sci. Technol.* **2023**, *20*, 13995–14032. [CrossRef]

Disclaimer/Publisher's Note: The statements, opinions and data contained in all publications are solely those of the individual author(s) and contributor(s) and not of MDPI and/or the editor(s). MDPI and/or the editor(s) disclaim responsibility for any injury to people or property resulting from any ideas, methods, instructions or products referred to in the content.